Earth and Planetary Science Letters 404 (2014) 22–32

Contents lists available at ScienceDirect

Earth and Planetary Science Letters

www.elsevier.com/locate/epsl

Neoproterozoic cap-dolostone deposition in stratified glacial meltwater plume

Chao Liu [a,*], Zhengrong Wang [a,*], Timothy D. Raub [b], Francis A. Macdonald [c], David A.D. Evans [a]

[a] Department of Geology and Geophysics, Yale University, P.O. Box 208109, New Haven, CT 06520, USA
[b] Department of Earth and Environmental Sciences, University of St Andrews, St Andrews, KY16 9AL, Scotland, UK
[c] Department of Earth and Planetary Sciences, Harvard University, Cambridge, MA 02138, USA

ARTICLE INFO

Article history:
Received 3 March 2014
Received in revised form 3 June 2014
Accepted 25 June 2014
Available online xxxx
Editor: G.M. Henderson

Keywords:
cap dolostones
Sr isotopes
Mg isotopes
Snowball Earth
plumeworld

ABSTRACT

Neoproterozoic cap carbonates host distinctive geochemical and sedimentological features that reflect prevailing conditions in the aftermath of Snowball Earth. Interpretation of these features has remained contentious, with hypotheses hinging upon timescale and synchronicity of deposition, and whether or not geochemical signatures of cap carbonates represent those of a well-mixed ocean. Here we present new high-resolution Sr and Mg isotope results from basal Ediacaran cap dolostones in South Australia and Mongolia. Least-altered Sr and Mg isotope compositions of carbonates are identified through a novel incremental leaching technique that monitors the purity of a carbonate sample and the effects of diagenesis. These data can be explained by the formation of these cap dolostones involving two chemically distinct solutions, a glacial meltwater plume enriched in radiogenic Sr, and a saline ocean residue with relatively lower $^{87}Sr/^{86}Sr$ ratios. Model simulations suggest that these water bodies remained dynamically stratified during part of cap-dolostone deposition, most likely lasting for ~8 thousand years. Our results can potentially reconcile previous conflicts between timescales estimated from physical mixing models and paleomagnetic constraints. Geochemical data from cap carbonates used to interpret the nature of Snowball Earth and its aftermath should be recast in terms of a chemically distinct meltwater plume.

1. Introduction

The demise of the Marinoan Snowball Earth (Kirschvink, 1992; Hoffman et al., 1998) around 635–636 Ma (Hoffmann et al., 2004; Condon et al., 2005; Calver et al., 2013) was associated with one of the largest perturbations of ocean chemistry and climate in Earth's history. Interpretations on the aftermath of this event come from the study of the meter- to decameter-thick cap dolostones deposited globally above Marinoan glacial diamictites (e.g. Hoffman et al., 1998; Hoffman, 2011b). Several hypotheses have been put forward to explain the stratigraphy, sedimentology and geochemistry of cap dolostones, including diachronous deglaciation of a 'Snowball Earth' (Hoffman et al., 2007; Rose and Maloof, 2010), gas–hydrate destabilization (Kennedy et al., 2001b, 2008; Jiang et al., 2003), 'plumeworld' (Shields, 2005), a.k.a. 'Glacial Lake Harland' (Hoffman, 2011a), and prolonged cyclical transgression (Kennedy and Christie-Blick, 2011). Discrepancies among these hypotheses originate mostly from the following two causes. First, the temporal evolution of the cap-dolostone deposition is poorly constrained. The timescale of cap-dolostone deposition in different sections is estimated to vary from ~4 thousand years (kyrs) (Hyde et al., 2000) to >100 kyrs (Raub, 2008; Font et al., 2010), and their relative temporal relationship is proposed to be isochronous (i.e. the bases and tops of the carbonate sequences are of the same ages in different sections, Kennedy et al., 2001b, 2008), semi-diachronous (i.e. bases are of different ages in different sections, while tops are of the same age, Shields, 2005), or diachronous (i.e. neither bases nor tops have the same age in different sections, Hoffman et al., 2007; Rose and Maloof, 2010). Second, it is unclear if these deposits formed within a well-mixed global ocean. All hypotheses proposed are consistent with the observed negative carbon-isotope excursions (e.g. Hoffman and Schrag, 2002; Kennedy and Christie-Blick, 2011; Kennedy et al., 2001b; Shields, 2005), which could be explained by variations of global (Hoffman and Schrag, 2002; Hoffman et al., 2007) or local carbon cycles in well-mixed seawater (Higgins and Schrag, 2003) or a stratified ocean (Shields, 2005; Hoffman, 2011a). Thus, other reliable and widespread geochemical

* Corresponding authors.
E-mail addresses: chao.liu@yale.edu (C. Liu), zhengrong.wang@yale.edu (Z. Wang).

http://dx.doi.org/10.1016/j.epsl.2014.06.039
0012-821X/

paleo-proxies within cap dolostones (Jacobsen and Kaufman, 1999; Halverson et al., 2007) are necessary to distinguish among these hypotheses.

Concentration ratios and isotopic compositions of several elements (e.g. Li, Mg, Ca and Sr) could help to address these issues. First, these elements are better mixed than dissolved inorganic carbon species in the ocean, as demonstrated by less spatial variability of their isotopic signatures than carbon isotopes in modern seawater (e.g. Hodell et al., 1990; Berner and Berner, 2012; Huh et al., 1998; Fantle and DePaolo, 2005). The residence times of Sr and Mg in the modern ocean are at least four orders of magnitude longer than that of carbon (e.g. Hodell et al., 1990; Berner and Berner, 2012), and it has been proposed that Sr residence time in the Neoproterozoic ocean may be even longer (Higgins and Schrag, 2003). Second, seawater Sr and Mg isotope compositions are determined by only a few (albeit different) processes, with $^{87}Sr/^{86}Sr$ ratios elevated by continental weathering and reduced through hydrothermal exchange (e.g. Davis et al., 2003; Vance et al., 2009; Allegre et al., 2010), and $\delta^{26}Mg$ increased by silicate weathering and carbonate precipitation (Tipper et al., 2006). Both Sr and Mg isotopes could trace enhanced continental weathering (e.g. Tipper et al., 2006; Halverson et al., 2007; Vance et al., 2009; Hoffman, 2011a) after 'Snowball Earth'. In this study, we report Mg isotope compositions of basal Ediacaran cap dolostones from Nuccaleena Formation (Fm) in South Australia, and Sr and Mg isotope compositions of cap dolostones from the Ol Fm of Mongolia. Along with the Sr isotope compositions of Nuccaleena Fm in South Australia (Liu et al., 2013), these data help constrain post-'Snowball Earth' paleoceanography.

2. Material and methods

2.1. Samples

Samples were collected from Nuccaleena Fm in South Australia, and the Ol Fm of the Tsagaan Olom Group in Mongolia (cf. Fig. S1 in supplemental information for detailed geological maps), both of which are cap carbonates formed after the Marinoan "Snowball Earth" (Macdonald et al., 2009; Rose and Maloof, 2010). The Nuccaleena samples were collected at Elatina Creek, where the cap dolostone is better preserved than most other sections in the Adelaide Rift Complex (McKirdy et al., 2001; Raub et al., 2007; Rose and Maloof, 2010). The basal contact of the Nuccaleena Fm with underlying proglacial siliciclastic deposits of the Elatina Fm is gradational (Raub et al., 2007). The Nuccaleena Fm is composed predominantly of recrystallized, pink- to buff-colored, coarse-grained peloidal dolomicrite (Lamb et al., 2012). In the lowest continuous dolostone beds, the Nuccaleena is medium-grained (0.2–0.5 mm) with mm-scale laminae that form cm-scale swaley, low-angle cross-stratification (Rose and Maloof, 2010) and coarsen upward into beds hosting m-scale trochoidal ripples that have been interpreted either as high-energy giant wave ripples (Allen and Hoffman, 2005) or low-energy deposits formed by early-cementation of coarse, low-density grains on inherited topography in an oscillatory flow regime (Lamb et al., 2012). In the upper part of the mega-rippled interval, mm-scale siltstone laminations inconsistently appear at cm- to dm-scale intervals. At the top the Nuccaleena Fm, a final megaripple is onlapped by fine-grained red siltstone of the Brachina Fm. The whole sedimentary package, from the base of a regionally-extensive flaser-bedded sandstone of the uppermost Elatina Fm (Raub et al., 2007) to the top of solid cap dolostone in Nuccaleena Formation, has been interpreted as a transgressive systems tract (Preiss, 2000). Overlying the cap dolostone, the Brachina Fm consists of a thick succession (>800 m) of upward-shoaling siltstone and minor sandstone, further supporting a flooding surface somewhere immediately above the highest bed of solid cap dolostone (Christie-Blick et al., 1995).

The Ol Fm was deposited above discontinuous wedges of lodgement till in the Khongor Fm. A glacial origin of the Khongor Fm is demonstrated by the presence of striated clasts, and cobble-sized dropstones that are suspended in a weakly-bedded shale matrix (Macdonald, 2011). The Ol cap dolostone sharply overlies the Khongor diamictite and consists of 5–40 m of buff to pink-colored, largely recrystallized micropeloidal dolostone with tubestone stromatolites, giant wave ripples, aragonite fans, and barite fans and breccia (Hoffman et al., 2011; Macdonald, 2011). The section transgresses upward into limestone ribbonite, gray rhythmite, and then ~5 m of iron-rich siltstone interbedded with marly carbonate, approximating the maximum flooding surface.

Terrigenous material is abundant in the Nuccaleena Fm, including detrital hematite and rutile, potassic and magnesian clays, quartz and trace apatite (Raub et al., 2007). In comparison, the Mongolian succession is carbonate-dominated, and siliciclastic material is extremely rare in the Ol cap dolostone (Macdonald et al., 2009). This can be explained by their contrasting depositional settings: Nuccaleena Fm deposited at a relatively shallow depth along the passive margin of a continental embayment (i.e. a marine embayment, Rose and Maloof, 2010), whereas Ol formed as an isolated carbonate platform on a submerged, distant, isolated ribbon continent (Fig. 3; Macdonald et al., 2009).

2.2. Analytical methods

Samples were analyzed for Mg and Sr isotope compositions and element concentrations (including Mg, Sr, Ca, Fe, Mn, and Rb). Immersed in ethanol, they were first crushed and ground into 100-mesh powder in an agate mortar. The powder (~200 mg) of each sample was then transferred into a centrifuge tube and leached at 20 °C following a 15-step leaching procedure, including 2 steps of 5 mL 1 M ammonium acetate (steps N1 and N2), 7 steps of 5 mL 0.25 vol% acetic acid (steps S1–S7), 3 steps of 6 mL 1 vol% acetic acid (steps S8–S10), 2 steps of 3 mL 5 vol% acetic acid (steps S11 and S12) and a final step of 6 mL 10 vol% acetic acid (S13) (Liu et al., 2013). This method has been demonstrated to be capable of minimizing the contamination from ion-exchange sites of clay minerals, altered carbonate and other mineral phases (Liu et al., 2013). In each step, sample tubes sat in a supersonic bath for 10 min, and then were centrifuged at 3600 rpm for 5 min. The supernatant was collected for elemental and isotopic analyses, while the residue was kept for further leaching. Geochemical measurements were conducted on leachates from all steps of selected samples (4 from Nuccaleena formation and 2 from Ol formation), and the four steps (S9–S12) of remaining samples, where least-altered dolomite phases are leached out (Liu et al., 2013). Geochemical measurements were also conducted on solutions of bulk carbonates. The powder of each sample (~20 mg) was washed by 5 mL 1 M ammonium acetate twice to remove the adsorbed contaminants, and then dissolved by ~8 mL of 10% (v/v) HAc in a supersonic bath for 10 min. The leaching residues were dried first and then weighed to estimate the amount of non-carbonate constituents in the sample (mostly clay minerals).

All measurements of isotopic ratios and element concentrations were conducted at Yale University using MC-ICP-MS (NEPTUNE) and single-collector ICP-MS (Element-XR), respectively. The analytical details of Sr-isotope compositions and element concentrations were described in the previous study (Liu et al., 2013). In this study, however, we employ a different strategy for mass-bias correction. In Liu et al. (2013), mass bias was corrected by using stable isotope ratio of $^{88}Sr/^{86}Sr = 8.375209$ assuming that its fractionation in MC-ICP-MS obeys an exponential law, which is common but not universally valid (e.g. Albarède et al., 2004).

In this study, we correct the mass bias using $^{87}Sr/^{86}Sr = 0.71025$ for NBS-987 and $^{87}Sr/^{86}Sr = 0.709175$ for our modern seawater/coral standards, that passed through ion exchange columns along with cap dolostone samples. This normalization showed varied mass-discrimination factors that are dependent on experimental conditions and instrumental configurations. Using the new approach, our standards are within ±0.00002 from the accepted value (i.e., $^{87}Sr/^{86}Sr = 0.71025 \pm 0.00002$ for NBS-987 and $^{87}Sr/^{86}Sr = 0.709175 \pm 0.00002$ for our modern seawater/coral standards). This technically improved normalization approach employed here does not affect interpretations in Liu et al. (2013), since the corrections are much smaller than the differences among various groups of samples.

Mg isotope compositions were reported as δ^{26}Mg values, relative to pure magnesium metal provided by Dead Sea Magnesium Ltd., Israel (Galy et al., 2003), which are in units of per mil defined as $[(R_{sample}/R_{standard}) - 1] \times 10^3$, where $R = {}^{26}Mg/{}^{24}Mg$. The analytical method for Mg isotope analysis followed the previous procedure established at Yale University (Wang et al., 2013) with an additional step to remove Fe from the solution. An aliquot of the samples was dried first, and then dissolved in HCl and passed through one anion exchange column (Biorad AG1-X8), one cation exchange column (Biorad AG50W-X8) and then another cation exchange column (Biorad AG50W-X12) to purify Mg in the geochemical clean lab. Pure Mg was dissolved in 5 wt% HNO_3 (ρ = 1.020 g/mL) for isotopic analyses using NEPTUNE. About 0.7 µg of Mg was used for measuring each solution three times and the typical blank in the experiments is about 0.2 ppb (or ~0.7 ng in 3.5 mL solution). During the measurements, every two samples were bracketed by at least one of the three in-house standards with known $\delta^{26}Mg_{DSM3}$ (‰) values (calibrated against DSM3) to monitor system stability. Typically four groups (totally 16 samples and 12 standards) make up a sequence for one-day measurement. Instrumental drift is monitored and corrected by the bracketing standards.

3. Results

3.1. Mg isotope variations in Nuccaleena cap dolostone

Mg isotope compositions of the supernatant from each leaching step of four selected samples (NUEL-6, NUEL-37, NUEL-100 and NUEL-123) are listed in Table 1 and shown in Fig. 1. The $^{87}Sr/^{86}Sr$ and element ratios of these samples have been previously reported in Liu et al. (2013). In all samples, the δ^{26}Mg values of cap dolostones are similar to each other in most leaching steps, except in the first few ones where dissolution of secondary calcite is dominated (indicated by low Mg/Ca ratios). The roughly-constant δ^{26}Mg values in most leaching steps imply that later alteration events would not alter δ^{26}Mg values of dolomite after they were formed, consistent with Geske et al. (2012). In addition, the small difference in δ^{26}Mg values between bulk samples and supernatants from a majority of leaching steps indicates that there is no isotopic fractionation introduced by leaching.

The profile of δ^{26}Mg values measured in this study is listed in Table 2 and plotted in Fig. 2A. The δ^{26}Mg values from the supernatants that have Rb-decay corrected, minimum $^{87}Sr/^{86}Sr$ ratios (RMSr ratios, i.e., the step where least-altered phases are dominantly leached out, Liu et al., 2013; Note that Rb-decay correction decreases the minimum $^{87}Sr/^{86}Sr$ values for less than 0.0002) are plotted. The δ^{26}Mg profile starts with a low value (−2.22‰) at the bottom, rises to −1.79‰ in the middle, and then decreases to −1.97‰ at the top of the Nuccaleena Formation (see Table 3).

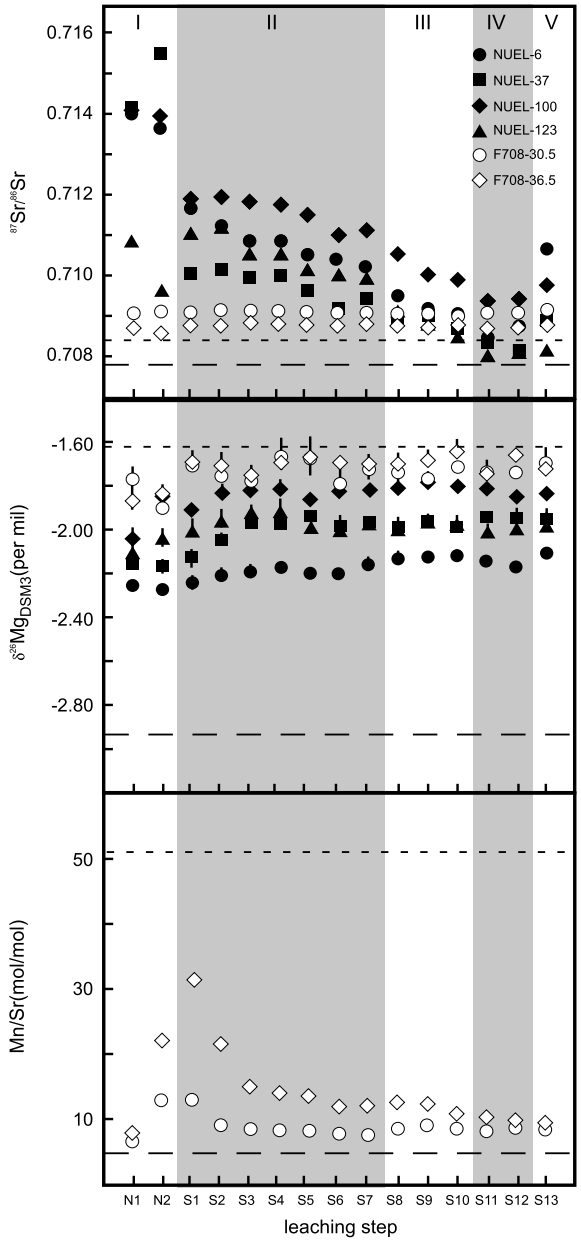

Fig. 1. Step-leaching results of $^{87}Sr/^{86}Sr$ (before Rb-decay correction), $\delta^{26}Mg_{DSM3}$ (‰) and Mn/Sr values for selected samples from Nuccaleena (solid symbols) and Ol formations (empty symbols). Short dashed lines: geochemical signatures of least-altered dolomite in partly-dolomitized Ol limestones; Long dashed lines: average geochemical signatures of Ol limestones. $^{87}Sr/^{86}Sr$ data for Nuccaleena samples are from Liu et al. (2013).

3.2. Sr and Mg isotope variations in the Ol Formation

The isotopic compositions of Sr and Mg in all leaching solutions of two selected samples (F708-30.5 and F708-36.5) of Ol cap dolostone are listed in Tables 1 and 2, and plotted in Fig. 1. Unlike those in Nuccaleena Fm, $^{87}Sr/^{86}Sr$ ratios of Ol cap dolostone exhibit little variations in all leaching steps, implying either the Ol cap dolostone was not affected by diagenesis or it was completely homogenized by a later alteration event. The δ^{26}Mg values of these samples also vary little in most leaching steps.

Elemental molar ratios of Mg/Ca, Sr/Ca, Fe/Ca, Mn/Sr and Rb/Sr in step-leached solutions of these two samples are also listed in Table 2. Irrespective of results from the first two steps (N1 and N2) where surface-adsorbed phases were leached out (Liu et al., 2013), the molar ratios of Sr/Ca, Fe/Ca and Rb/Sr in other steps exhibit

Table 1
$\delta^{26}Mg_{DSM3}$ (‰) values of all leaching steps of selected cap dolostones.

Step	South Australia				Mongolia		
	NUEL-6	NUEL-37	NUEL-100	NUEL-123	F708-30.5	F708-36.5	F708-44
N1	−2.24(2)	−2.15(2)	−2.03(5)	−2.10(2)	−1.76(4)	−1.86(6)	−1.98(8)
N2	−2.26(1)	−2.16(3)	−1.84(2)	−2.03(6)	−1.89(5)	−1.82(1)	−2.61(5)
S1	−2.23(3)	−2.12(6)	−1.90(1)	−2.00(6)	−1.70(2)	−1.68(3)	−3.10(4)
S2	−2.20(2)	−2.04(1)	−1.82(2)	−1.95(6)	−1.75(4)	−1.70(5)	−3.13(4)
S3	−2.18(2)	−1.96(2)	−1.81(2)	−1.91(3)	−1.77(3)	−1.74(3)	−3.16(7)
S4	−2.16(2)	−1.97(1)	−1.80(2)	−1.91(5)	−1.66(8)	−1.69(3)	−2.98(3)
S5	−2.19(1)	−1.93(1)	−1.85(1)	−1.98(2)	−1.67(9)	−1.66(3)	−2.99(1)
S6	−2.19(1)	−1.98(3)	−1.82(2)	−2.00(2)	−1.78(6)	−1.68(5)	−3.03(3)
S7	−2.15(2)	−1.96(1)	−1.81(1)	−1.96(2)	−1.72(6)	−1.69(1)	−2.95(2)
S8	−2.12(1)	−1.98(2)	−1.80(2)	−2.00(3)	−1.73(8)	−1.69(2)	−2.01(3)
S9	−2.11(1)	−1.95(1)	−1.77(2)	−1.95(2)	−1.76(3)	−1.67(3)	−1.71(2)
S10	−2.11(2)	−1.98(2)	−1.79(1)	−1.96(2)	−1.71(1)	−1.64(4)	−1.62(4)
S11	−2.13(1)	−1.93(1)	−1.80(1)	−2.00(1)	−1.72(2)	−1.73(5)	−1.83(4)
S12	−2.16(3)	−1.94(3)	−1.84(1)	−1.99(2)	−1.74(2)	−1.68(4)	−1.56(3)
S13	−2.11(2)	−1.94(2)	−1.82(1)	−1.97(4)	−1.69(6)	−1.72(2)	−1.50(3)
Bulk	−2.16(4)	−1.96(3)	−1.81(3)	−1.96(2)	−1.74(4)	−1.71(3)	–

Note that the number within the parentheses in all figures represents the 1σ variation in the last digit. Same as in the following tables.

Table 2
$^{87}Sr/^{86}Sr$ (before Rb-decay correction) and trace metal ratios of all leaching steps of selected samples from Ol cap dolostones, Mongolia.

Step	F708-30.5					F708-36.5				
	$^{87}Sr/^{86}Sr$	Mg/Ca (mol/mol)	Sr/Ca (μmol/mol)	Mn/Sr (mol/mol)	Rb/Sr (mmol/mol)	$^{87}Sr/^{86}Sr$	Mg/Ca (mol/mol)	Sr/Ca (μmol/mol)	Mn/Sr (mol/mol)	Rb/Sr (mmol/mol)
N1	0.70929(3)	0.46(5)	310(16)	6.2(13)	4.95(44)	0.70919(3)	0.17(4)	230(10)	7.9(12)	8.19(63)
N2	0.70928(2)	0.57(6)	322(20)	12.6(14)	1.92(31)	0.70895(3)	0.30(3)	188(9)	19.8(15)	2.69(30)
S1	0.70923(2)	0.79(2)	356(7)	13.0(3)	0.16(5)	0.70874(2)	0.30(1)	163(3)	31.9(7)	0.55(8)
S2	0.70926(3)	0.84(2)	374(7)	9.4(3)	0.33(5)	0.70881(2)	0.55(1)	193(4)	20.5(5)	0.81(9)
S3	0.70925(2)	0.86(2)	383(7)	8.5(3)	0.43(5)	0.70886(3)	0.63(2)	203(5)	14.9(6)	1.83(15)
S4	0.70923(2)	0.87(3)	387(10)	8.6(5)	0.76(10)	0.70891(2)	0.64(2)	200(5)	15.1(7)	5.69(28)
S5	0.70924(3)	0.90(3)	381(9)	8.4(5)	0.93(9)	0.70895(2)	0.71(2)	213(6)	13.4(8)	6.26(34)
S6	0.70925(2)	0.87(3)	392(11)	8.1(5)	1.03(12)	0.70897(3)	0.79(3)	216(7)	12.0(9)	4.59(29)
S7	0.70925(3)	0.89(4)	397(12)	7.7(6)	0.95(12)	0.70897(2)	0.78(3)	216(7)	12.1(10)	4.46(32)
S8	0.70923(2)	0.91(2)	395(8)	8.5(3)	0.48(7)	0.70892(2)	0.74(1)	209(4)	12.6(4)	2.12(9)
S9	0.70923(2)	0.92(2)	404(9)	8.9(4)	0.31(6)	0.70895(2)	0.81(2)	232(4)	12.8(4)	2.44(11)
S10	0.70924(2)	0.91(4)	397(12)	8.5(6)	0.56(11)	0.70895(3)	0.88(2)	229(4)	10.9(4)	1.87(8)
S11	0.70923(3)	0.91(2)	399(7)	7.9(2)	0.78(5)	0.70900(2)	0.89(2)	222(4)	10.6(4)	2.08(9)
S12	0.70924(2)	0.89(2)	376(7)	8.6(2)	0.51(4)	0.70902(2)	0.87(2)	228(4)	9.8(3)	2.19(9)
S13	0.70912(2)	0.99(2)	377(7)	8.1(2)	0.29(1)	0.70901(2)	0.95(2)	232(4)	9.4(2)	1.81(6)

small variations with progressive leaching. Mg/Ca molar ratios increase rapidly in the first few steps (steps S1 through S4), reach a plateau in the middle-to-late steps (steps S5 through S12 having Mg/Ca of ∼0.8–0.9), with a moderate jump to ∼1.0 in the last step (S13). In contrast, Mn/Sr molar ratios display an opposite trend, with high values in the first few steps, dropping rapidly and reaching a plateau in the middle-to-last steps. These variations indicate secondary calcite was leached out first, followed by altered and less-altered dolomite, similar to Nuccaleena samples (Liu et al., 2013).

RMSr (usually at step S11 and with differences less than 0.0001 compared to other steps) in each Ol cap-dolostone sample is selected to reconstruct the stratigraphic profile of $^{87}Sr/^{86}Sr$, which has a similar $^{87}Sr/^{86}Sr$ value to most leaching steps and the bulk sample. Note that Rb-decay correction decreases $^{87}Sr/^{86}Sr$ for less than 0.00005. The $^{87}Sr/^{86}Sr$ ratios of all Ol cap dolostones exhibit comparatively less variations (0.7088–0.7093, average 0.7091 ± 0.0001, Table 4 and Fig. 2B). Similarly, the stratigraphic profile of $\delta^{26}Mg_{DSM3}$ values of the leaching step 11 in each sample (Fig. 2B), shows relatively small variations as well (i.e. $-1.64 \sim -1.84$‰, average -1.73 ± 0.05‰).

Elemental molar ratios (including Mg/Ca, Sr/Ca and Mn/Sr) of the supernatants with the RMSr ratio in each sample are listed in Table 4. Mg/Ca ratios are roughly constant (0.85–0.89 mol/mol, except for one data point as high as 1.11), Sr/Ca are between 0.2 and 0.4 mmol/mol (corresponding to ∼100–200 ppm Sr), Fe/Ca are between 2.2 and 7.9 mmol/mol and Mn/Sr are between 7.5 and 31 mol/mol.

Besides cap dolostones, we also analyzed limestones overlying cap dolostones. Their $^{87}Sr/^{86}Sr$, $\delta^{26}Mg$ and trace elemental ratios are reported in Table S1 and described in supplemental information (SI).

4. Discussion

4.1. Interpretations of Sr and Mg isotopes in cap dolostones

The Nuccaleena cap dolostones can be divided into two groups based on their RMSr ratios (Liu et al., 2013): 1) Group-I Nuccaleena cap dolostones (NG-I), with an average value of 0.7077 ± 0.0003 (1σ); and 2) Group-II Nuccaleena cap dolostones (NG-II), with an average ratio of 0.7092 ± 0.0003 (1σ), which is statistically indistinguishable from the average RMSr ratio of Ol cap dolostones (0.7091 ± 0.0001, 1σ, Fig. 2).

The supernatants in leaching steps having the RMSr ratios originate from dissolution of the least-altered carbonate (Liu et al., 2013). Because the minimum RMSr ratios (∼0.7073) of NG-I cap dolostones are within the range of, or slightly higher than, primary $^{87}Sr/^{86}Sr$ values reported for pre- and post-glacial limestone (Halverson et al., 2007; Kennedy et al., 1998) and barite (Shields et al., 2007), they should have formed in a solution related to penecontemporaneous seawater (Liu et al., 2013). In contrast, the

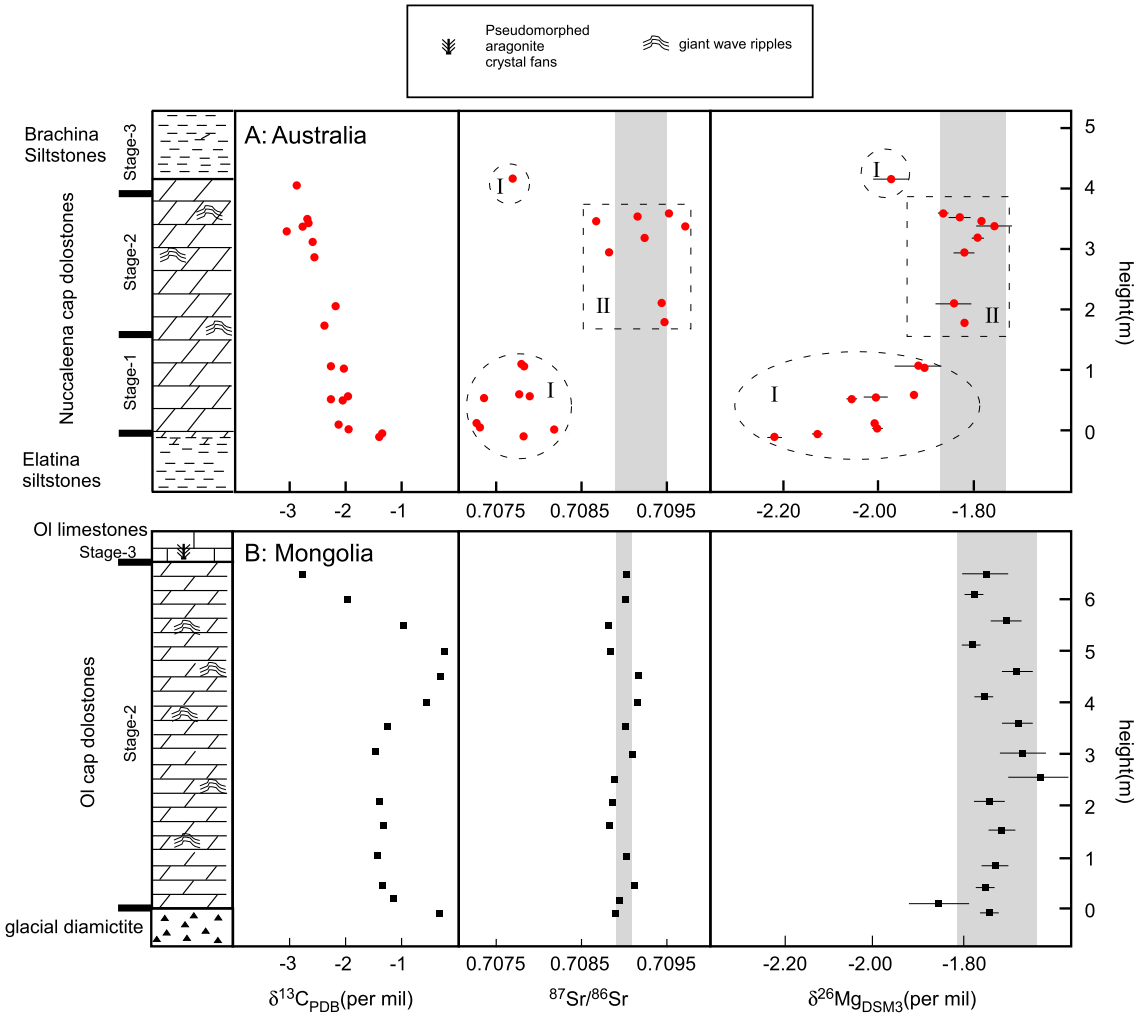

Fig. 2. Carbon, Sr and Mg isotope profiles of the Nuccaleena and Ol cap dolostones: A: $\delta^{13}C_{PDB}$ (‰), $^{87}Sr/^{86}Sr$ (Rb-decay corrected) and $\delta^{26}Mg_{DSM3}$ (‰) of the Nuccaleena Formation; B: $\delta^{13}C_{PDB}$ (‰), $^{87}Sr/^{86}Sr$ and $\delta^{26}Mg_{DSM3}$ (‰) of the Ol cap dolostones. Nuccaleena samples are categorized into two groups (I and II) based on their $^{87}Sr/^{86}Sr$ values, and they form in three different stages (Stage 1, Stage 2 and Stage 3, see the text for discussion). Ol cap dolostones are exclusively formed during Stage 2. The grey bands show the average Mg and Sr isotopic values of cap dolostones formed during Stage 2, with 1σ standard deviations. Carbon isotope data are from Macdonald et al. (2009) and Raub (2008).

Table 3
$\delta^{26}Mg_{DSM3}$ (‰) values of Nuccaleena cap dolostones, South Australia. The values of both bulk carbonate and the leaching step with lowest $^{87}Sr/^{86}Sr$ in each sample are reported, together with the carbonate concentration in these samples.

Sample	Height (m)	Carb (wt%)	Bulk	Least altered	Group-II				
					Sample	Carb (wt%)	Height (m)	Bulk	Least altered
NUEL-4	−0.085	72	−2.24(6)	−2.22(1)	NUEL-52	85	1.78	−1.90(1)	−1.82(1)
6	−0.04	78	−2.16(4)	−2.13(4)	61	90	2.11	−1.93(2)	−1.84(4)
134	0.05	79	−2.11(2)	−2.00(1)	83	87	2.94	−1.91(1)	−1.83(2)
136	0.12	77	−2.09(5)	−2.01(3)	90	83	3.18	−1.77(1)	−1.80(1)
18	0.53	80	−2.08(3)	−2.06(3)	96	86	3.37	−1.76(3)	−1.75(4)
19	0.56	84	−2.01(2)	−2.01(3)	98	88	3.45	−1.82(2)	−1.79(1)
20	0.6	80	−1.98(2)	−1.94(1)	100	87	3.52	−1.81(2)	−1.84(1)
37	1.05	86	−1.96(3)	−1.93(1)	102	83	3.58	−1.92(2)	−1.87(1)
38	1.08	84	−1.99(1)	−1.97(3)					
123	4.15	87	−1.96(2)	−1.97(4)					

elevated RMSr ratios shared by NG-II and Ol cap dolostones could be explained by at least two different possibilities: 1) cap dolostones from both stratigraphic intervals experienced local alteration events that coincidentally elevated the RMSr ratios to a similar value (Liu et al., 2013); or 2) both intervals formed in a widespread water body (i.e. glacial meltwater as in 'plumeworld', Shields, 2005 or 'Glacial Lake Harland', Hoffman, 2011a) with a higher $^{87}Sr/^{86}Sr$ ratio than that of penecontemporaneous seawater at depth.

The $\delta^{26}Mg_{DSM3}$ values in leaching steps with the RMSr ratios range from −2.22 to −1.75‰ in Nuccaleena cap dolostones (Fig. 2A) and are less variable in the Ol cap dolostones (−1.73 ± 0.08‰, 1σ, Fig. 2B), which, interestingly, resembles those of NG-II cap dolostones (averagely −1.80 ± 0.07‰, 1σ). Interpretation of

Table 4
$^{87}Sr/^{86}Sr$ (Rb-decay corrected), $\delta^{26}Mg_{DSM3}$ (‰) and trace metal ratios of Ol cap dolostones, Mongolia. The values of the leaching step S11 are selected to represent each sample.

Sample	$^{87}Sr/^{86}Sr$	$\delta^{26}Mg_{DSM3}$ (‰)	Mg/Ca (mol/mol)	Sr/Ca (μmol/mol)	Fe/Ca (mmol/mol)	Mn/Sr (mol/mol)	Rb/Sr (mmol/mol)
F708-29.7	0.70904(2)	−1.75(2)	0.89(3)	243(6)	4.4(2)	14.1(9)	1.32(9)
30.2	0.70922(2)	−1.72(5)	0.89(4)	335(7)	3.7(2)	8.2(4)	0.43(6)
30.5	0.70920(3)	−1.72(2)	0.91(2)	399(7)	2.4(1)	7.9(2)	0.78(5)
31.0	0.70916(2)	−1.76(3)	0.89(2)	385(5)	2.4(1)	8.7(3)	0.31(4)
31.5	0.70899(2)	−1.73(1)	0.90(2)	379(8)	2.2(1)	7.8(7)	0.45(3)
32.0	0.70900(2)	−1.79(2)	0.87(4)	389(4)	2.5(1)	7.6(6)	0.58(6)
32.5	0.70905(2)	−1.84(6)	0.86(2)	357(6)	7.6(3)	7.5(6)	0.45(7)
33.0	0.70919(1)	−1.70(3)	0.90(2)	406(8)	2.2(1)	8.3(4)	0.35(9)
33.5	0.70920(2)	−1.71(6)	0.88(3)	308(4)	4.1(2)	12.5(7)	0.43(8)
34.0	0.70926(2)	−1.64(5)	0.90(1)	291(7)	4.4(2)	13.8(4)	1.65(10)
34.5	0.70928(2)	−1.69(7)	0.89(3)	343(7)	3.5(2)	15.4(5)	0.99(8)
35.0	0.70895(2)	−1.76(10)	0.90(2)	242(6)	6.2(3)	31.3(6)	0.99(9)
35.5	0.70893(2)	−1.67(7)	0.89(2)	185(5)	6.8(3)	23.3(8)	1.08(10)
36.0	0.70915(2)	−1.81(7)	1.12(3)	195(7)	7.9(4)	15.5(6)	1.53(8)
36.5	0.70895(2)	−1.73(5)	0.89(2)	222(4)	5.0(1)	10.6(4)	2.08(9)

measured $\delta^{26}Mg_{DSM3}$ values, however, is non-trivial, since the Mg isotope composition of dolomite ($\delta^{26}Mg_d$) depends on the Mg isotope composition of the coexisting solution ($\delta^{26}Mg_s$) from which dolomite formed (e.g. dolomitization fluids, Galy et al., 2002; or pore fluids, Higgins and Schrag, 2010), and the fractionation factor between dolomite and solution ($\delta^{26}Mg_{d-s} = \delta^{26}Mg_d - \delta^{26}Mg_s$) controlled by temperature (Galy et al., 2002; Saenger and Wang, 2014; Schauble, 2011; Wang et al., 2013) and/or by precipitation rate (e.g., Mavromatis et al., 2013; Saenger and Wang, 2014). The similarity in $\delta^{26}Mg_d$ values between dolomites in NG-II and Ol cap dolostones indicates that they could have formed in environments with similar $\delta^{26}Mg_s$ and $\delta^{26}Mg_{d-s}$ or with completely different $\delta^{26}Mg_s$ and $\delta^{26}Mg_{d-s}$ values but coincidently having a similar sum of $\delta^{26}Mg_s$ and $\delta^{26}Mg_{d-s}$.

Previously proposed mechanisms for cap-dolostone formation include direct precipitation, early dolomitization, deep burial dolomitization and late dolomitization (e.g. Fairchild and Kennedy, 2007, and literature reviewed therein). Although the similar Sr and Mg isotope values in both NG-II and Ol sections could be interpreted separately by these mechanisms, the concordant Mg and Sr isotope values favor the formation of the two sedimentary sections in the same water body (or well-connected water bodies), via direct precipitation or early dolomitization (e.g. Vasconcelos et al., 1995; Warren, 2000; Warthmann et al., 2000; Roberts et al., 2004; Sánchez-Román et al., 2008; Zhang et al., 2012) for the following reasons. First, during deep burial dolomitization, dolomite would exhibit ~0.7 (±0.2)‰ differences in $\delta^{26}Mg$, depending on the amount of clay minerals co-precipitated which preferentially incorporate ^{26}Mg (Higgins and Schrag, 2010). In our samples, we observed similar $\delta^{26}Mg$, but different amounts of clay minerals in NG-II and Ol cap dolostones (~10–30% vs. <1%, respectively, estimated from weights of leaching-residues). Although it is unclear whether the clay minerals in NG-II cap dolostones co-precipitated with dolomite, in other sections they have been interpreted as syn-sedimentary clays (Bristow et al., 2009). Second, the cap dolostones are also unlikely to have formed via late dolomitization because their chemistry (including Sr and Mg isotope compositions and element ratios such as Mn/Sr) is different from that of leachates in dolomite portions of the overlying partially-dolomitized limestone (Fig. 2 and SI). Finally, giant ripple structures present in most cap dolostones suggest extremely early cementation (Lamb et al., 2012), so that if early dolomitization occurred, the dolomitization fluids were likely in contact with the water body from which the original carbonates were precipitated.

During direct precipitation or early dolomitization, $\delta^{26}Mg_d$ values of cap dolostones would reflect the original $\delta^{26}Mg_s$ values of solution, the dolomite precipitation temperature and precipitation rates. Both Nuccaleena and Ol cap dolostones likely formed in warm, subtropical marine locales (e.g. Kravchinsky et al., 2010; Williams et al., 2011; Evans and Raub, 2011) and have similar stratigraphic thicknesses and sedimentary textures (Macdonald et al., 2009; Lamb et al., 2012), implying similar formation conditions (e.g. temperature and precipitation rates) and thus similar $\delta^{26}Mg_{d-s}$ values. Therefore, the similar $\delta^{26}Mg_d$ values of both cap dolostones suggest that they form from solutions sharing similar $\delta^{26}Mg_s$ values.

Unlike NG-II and Ol cap dolostones, much lower $\delta^{26}Mg_{DSM3}$ values is observed in the NG-I cap dolostones (Fig. 2A), monotonically increasing from −2.22‰ (±0.01, 1σ) to −1.91‰ (±0.03, 1σ). As discussed above, this could be explained by the increase in $\delta^{26}Mg_s$ and/or $\delta^{26}Mg_{d-s}$ (note $\delta^{26}Mg_{d-s} < 0$, so that the increase in $\delta^{26}Mg_{d-s}$ would indicate smaller absolute differences between dolomite and solution). Although the temperature sensitivity ($d\delta^{26}Mg_{d-s}/dT$) has yet to be calibrated experimentally, first-principle calculation predicts $\delta^{26}Mg_{d-s}$ shall increase (toward zero) with increasing temperature (Schauble, 2011). Moreover, $\delta^{26}Mg_{d-s}$ can be estimated to be higher than $\delta^{26}Mg_{magnesite-solution}$ (Pearce et al., 2012), but lower than $\delta^{26}Mg_{aragonite-solution}$ (Wang et al., 2013) based on the relative Mg–O bond strength (Schauble, 2011; Wang et al., 2013). Thus, $d\Delta^{26}Mg_{d-s}/dT$ can be estimated between 0.009 and 0.033‰/°C (Saenger and Wang, 2014). $\Delta^{26}Mg_{d-s}$ could also increase with increasing precipitation rates, as is manifested in Mg isotope fractionation between calcite and solution (Li et al., 2012; Mavromatis et al., 2013). Thus, the increase of $\delta^{26}Mg_d$ by ~0.3‰ in NG-I cap dolostones can be explained by the following reasons: 1) temperature increase by up to ~9–33 °C (increasing $\delta^{26}Mg_{d-s}$); 2) significant increase in precipitation rate for NG-II compared with NG-I cap dolostones (increasing $\delta^{26}Mg_{d-s}$); 3) gradual accumulation of ^{26}Mg-enriched glacial melt–water in the ocean from continental influx (increase $\delta^{26}Mg_s$); and 4) precipitation of a large amount of ^{26}Mg-depleted dolomite which can raise the $\delta^{26}Mg$ values of the ocean (since $\delta^{26}Mg_s > \delta^{26}Mg_d$). Moreover, if the dolostone formed through biological mediated process, the Mg isotope fractionation could conceivably be affected by the biological process, as shown in modern biogenic aragonite and calcite (e.g. Saenger and Wang, 2014). However, current knowledge is insufficient to distinguish among these possibilities.

4.2. A model for cap-dolostone deposition: 'plumeworld'

The geochemical similarities and differences between Nuccaleena and Ol cap dolostones, which likely formed remotely from each other (Hoffman and Li, 2009; Li et al., 2013), can be understood in the framework of 'plumeworld' model (Shields, 2005),

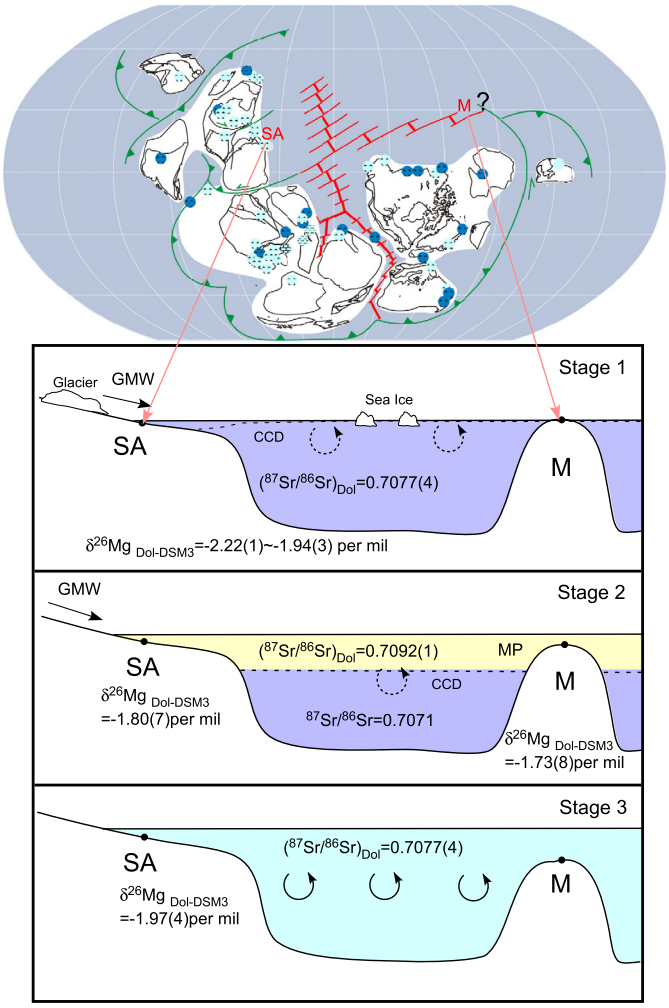

Fig. 3. Top panel: Paleogeographic reconstructions at ~635 Ma, adapted from Hoffman and Li (2009) and Li et al. (2013). M: Mongolia; SA: South Australia. Light blue circles: shallow marine deposits; Dark blue circles: deep marine deposits. Subduction and spreading zones are also plotted. Note that although the position of Mongolian terrane is not well constrained, it is still relatively distant from South Australia. Bottom panel: Schematic representation of the different stages of cap dolostones deposition. Stage 1: Carbonates only formed in areas next to large continents with abundant continental-weathering derived alkalinity input; Stage 2: the meltwater plume is formed. Carbonates are deposited throughout the plume; Stage 3: the plume is destabilized by ocean overturning. $^{87}Sr/^{86}Sr$ and $\delta^{26}Mg_{DSM3-Dol}$ (‰) values in each reservoir are also shown. CCD: carbonate compensation depth, represented by the dashed line; GMW: glacial melt water. (For interpretation of the references to color in this figure legend, the reader is referred to the web version of this article.)

divisible into one pre-stage and three main stages (Fig. 3). Prior to the formation of cap dolostones in Mongolia and Australia, increased concentrations of atmospheric greenhouse gases caused the climate to warm, glacial ice melted and rain-out diamictites were deposited (e.g. Hoffman et al., 1998; Hoffman and Schrag, 2002; Jiang et al., 2003; Kasemann et al., 2005; Bao et al., 2008). Buffered by ice–saline seawater mixture, the ocean was still cold, rich in dissolved CO_2 and thus more acidic than modern seawater (Higgins and Schrag, 2003; Kasemann et al., 2005), which would inhibit carbonate precipitation.

Cap dolostones began to form during Stage 1 at low latitudes (e.g., South Australia, Fig. 3), and as global climate continued to warm and continental icesheets decayed at higher latitudes, fresh meltwater continued to flush into the ocean. In relatively shallow and proximal marine embayments such as South Australia, the temperature increase and abundant continent-derived alkalinity input would have facilitated degassing of CO_2 and carbonate precipitation. Moreover, continent-derived nutrients (e.g. P and bio-essential trace metals) could promote the growth of organisms such as cyanobacteria, driving microbially-mediated carbonate production (e.g. Kunzmann et al., 2013; Shields, 2005; Van Lith et al., 2003; Vasconcelos and McKenzie, 1997; Warthmann et al., 2000). In contrast, along margins of distal terranes with less extensive subaerial sources (e.g. Mongolia), or at higher latitude, carbonate deposition could have been delayed by limited alkalinity input or due to different palaeo-bathymetric depths, as described in diachronous or semi-diachronous models (Shields, 2005; Hoffman et al., 2007; Rose and Maloof, 2010).

In Stage 1 the $^{87}Sr/^{86}Sr$ value of fluids involved in the deposition of NG-I cap dolostones can be inferred from the measured RMSr ratios (0.7077 ± 0.0003). The lack of a large RMSr variation in Stage-1 cap dolostones may result from a large oceanic Sr inventory (Higgins and Schrag, 2003). We suggest that the slight elevation of RMSr compared to contemporary seawater $^{87}Sr/^{86}Sr$ values (0.7071, Halverson et al., 2007) and measurable small variations of the RMSr ratios within NG-I cap dolostones (Fig. 2A) reflect dynamic mixing between seawater and fresh glacial melt water, or minor but variable contributions from non-carbonate minerals in different samples (Liu et al., 2013).

Inferring $\delta^{26}Mg$ values of seawater in Stage 1 is non-trivial, as discussed in Section 4.1. However, any one of the four possibilities accounting for the $\delta^{26}Mg_d$ increase is consistent with the scenario of a warming ocean receiving vast amounts of glacial meltwater. This increase of $\delta^{26}Mg_d$ is prominent at the very bottom, and attenuated in the upper reaches, of the studied Nuccaleena cap dolostones (Fig. 2A), implying that the more profound environmental change (e.g., solution chemistry and/or temperature) associated with Marinoan deglaciation was expressed, predictably, during earlier deglacial stages.

In Stage 2 (Fig. 3), warm and fresh continental glacial meltwater flushed into the ocean, possibly forming a widespread (Hoffman and Li, 2009; Li et al., 2013) plume, herein referred to as the 'Nuccaleena-Ol plume', dynamically stratified above cold saline seawater. The similar Sr and Mg isotopes shared by NG-II and Ol cap dolostones, suggests that isopycnal mixing of the stratified meltwater plume is efficient. We interpret both sections to have deposited synchronously in this plume as the carbonate compensation depth (CCD) rapidly deepened and sea level rose (consistent with the semi-diachronous model, Shields, 2005). The $^{87}Sr/^{86}Sr$ value of the meltwater plume as inferred from the RMSr ratios of NG-II and Ol cap dolostones exhibits small variations of ~0.7092 ($\pm 0.0003, 1\sigma$). However, this ratio is higher than pre- and post-glacial seawater $^{87}Sr/^{86}Sr$ values (Halverson et al., 2007; Kennedy et al., 1998), suggesting a significant amount of input from continental silicate weathering (e.g. Gaillardet et al., 1999; Vance et al., 2009; Allegre et al., 2010). Compared with $\delta^{26}Mg$ values of the basal NG-I cap dolostone in Stage 1, elevated but relatively uniform $\delta^{26}Mg$ values in NG-II and Ol cap dolostones are also consistent with enhanced continental silicate weathering input (Tipper et al., 2006), although they may reflect other factors including higher temperature/precipitation rates (Li et al., 2012; Mavromatis et al., 2013; Schauble, 2011) and/or larger proportions of dolomite (Tipper et al., 2006) formed in the plume than in seawater. Areal extent of the Nuccaleena–Ol plume is yet to be constrained, although paleogeography studies suggest that it is possibly more than several thousand kilometers wide (Hoffman and Li, 2009). It could be a global melt–water plume, or one of several regional plumes around the world. Least-altered geochemical signatures, especially Sr and Mg isotopes, of other Marinoan cap-dolostone sections could help to resolve this issue in future studies.

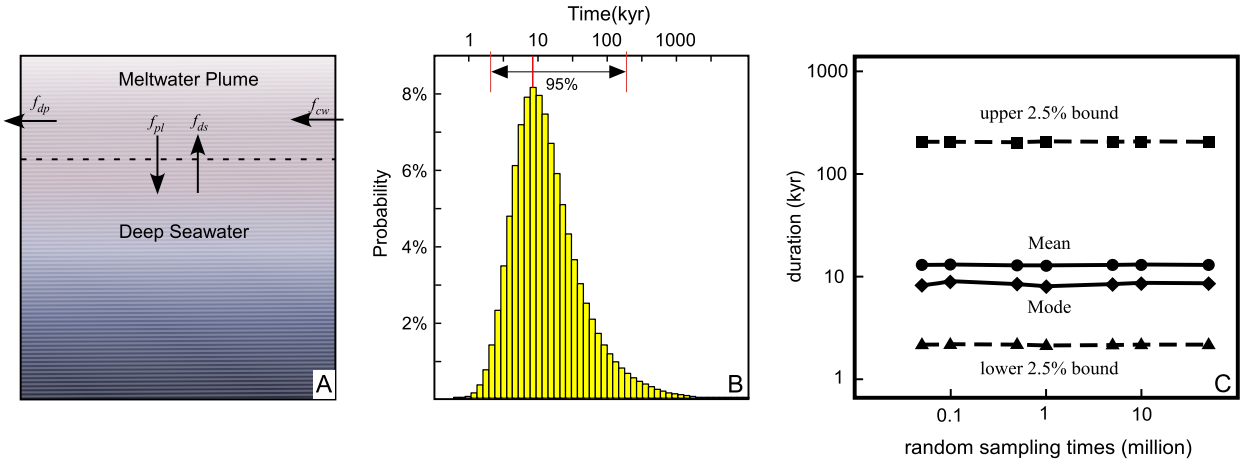

Fig. 4. A: Visual depiction of the geochemical box model. Possible Mg and Sr fluxes into and out of the plume include continental weathering input (f_{cw}), dolomite precipitation sink (f_{dp}), and the exchange of fluxes between deep seawater and the plume (f_{ds} and f_{pl}). B: The Monte-Carlo simulation result of the duration of the Stage-2 plume, exhibiting a mode of ~8 kyrs with a 95% confidence interval of 2.3 to 202 kyrs. C: A test of the model convergence. Four key factors of the modeling results, including the mean, mode, lower 2.5% percentile and higher 2.5% percentile of the distributions, are plotted for sampling sizes of 0.05, 0.1, 0.5, 1, 5, 10 and 50 million. All these factors are almost constant, indicating the converged modeling results.

In Stage 3 (Fig. 3), as the stratified ocean completely/partially overturned through several mechanisms (including turbulent diffusion, breaking waves, surface wind stirring, the establishment of global thermohaline circulation and ocean currents, and planetary tides), the final overturn of deep seawater would have inhibited dolomite precipitation (Shields, 2005; Hurtgen et al., 2006), as supported by the presence of pseudomorphosed aragonite crystal fans and limestones in the upper Ol Fm (Macdonald et al., 2009) and many other sections globally (Hoffman and Schrag, 2002; Fairchild and Kennedy, 2007). At this stage, $^{87}Sr/^{86}Sr$ ratios of the seawater returned to, or closely to those at the end of Stage 1, as recorded in the NG-I cap dolostones overlying the NG-II cap dolostones (Fig. 2A) and Ol limestones (~0.7079 on average, SI). This transition can be related to the upwelling of deep seawater with a low $^{87}Sr/^{86}Sr$ ratio and high concentration of Sr. Correspondingly, the $\delta^{26}Mg$ value of upper NG-I cap dolostones is similar to the range of values immediately underlying NG-II cap dolostones at the base of the Elatina Creek section (Fig. 2A). This similarity can be explained by the upwelling of Mg-rich, $\delta^{26}Mg$-low deep seawater, although other possibilities cannot be ruled out, including: 1) reduction in the amount of dolomite formation; 2) temperature decrease; and 3) slower dolomite formation.

4.3. Implication of the 'plumeworld' model for previous geochemical studies

The lack of significant differences in $^{87}Sr/^{86}Sr$ ratios between pre- and post-glacial seawater has been suggested to contradict the Snowball Earth hypothesis (Jacobsen and Kaufman, 1999; Kennedy et al., 2001a). However, there is an alternative explanation for the relatively constant seawater $^{87}Sr/^{86}Sr$ in the 'plumeworld' scenario. Although the Sr fluxes from the plume to deep seawater (f_{pl-Sr}, Fig. 4A) are not constrained, radiogenic Sr could be incorporated into cap dolostones within the plume before entering deep seawater, and seawater $^{87}Sr/^{86}Sr$ would remain unaltered despite significant continental weathering input during deglaciation.

Besides Sr–Mg isotope composition of cap dolostones, the 'plumeworld' implications of this study can also accommodate other published geochemical data. For example, the inorganic carbon isotope anomaly in Marinoan cap dolostones (Hoffman and Schrag, 2002) has been proposed to reflect a global temperature increase (Higgins and Schrag, 2003) and atmospheric CO_2 drawdown via continental silicate weathering (Hoffman et al., 1998). Variations in the magnitude of the carbon-isotope anomaly among cap dolostones from different localities were explained by a diachronous model (Hoffman et al., 2007). However, not all carbon-isotope data (e.g., Ol CDs in Fig. 2B, and some sections of Nuccaleena CDs, Rose and Maloof, 2010) can be fit to the diachronous model. We propose that these data could reflect contributions from local carbon sources/sinks that are not well mixed in the stratified plume, depending on the timescale of local processes, the mixing rate of the plume and the deposition rate of cap dolostones (as estimated in Section 4.4). In addition, these data could also reflect that carbon isotopes of some cap dolostones might be heterogeneous, as well as oxygen isotopes. Thus the bulk-carbonate C and O isotopic data cannot be simply correlated between different sections, or compared against RMSr and Mg isotopes. In these cases, RMSr and Mg isotopes are powerful tools for the regional and global chemostratigraphic correlations. Last but not least, besides Marinoan cap dolostones, the 'plumeworld' model could be potentially extended to Sturtian cap-carbonates, in which the elevated Os and Sr isotopes suggest mixing of radiogenic meltwater with seawater (Rooney et al., 2014).

4.4. Duration of the 'Plumeworld': A box-model exercise

Information about the duration of cap-dolostone deposition (or the deposition rate of cap dolostones) is essential to understanding the nature of deglaciation of Marinoan Snowball Earth and interpreting the geochemical data documented in cap dolostones. Due to the lack of a direct and sufficiently precise dating method, this information has long been debated (Shields, 2005; Hoffman et al., 2007; Font et al., 2010). Ocean circulation models calculate that ocean stratification will be destabilized in several thousand years (Zhang et al., 2001, 2002), a value previously adopted for the plume duration (Shields, 2005). Such a timescale (2–10 kyrs) has also been inferred for cap-dolostone deposition based on modeled rates for ice-sheet decay during deglaciation (Hoffman et al., 2007; Hyde et al., 2000), and geologic evidence that cap dolostones may be truncated in their middle by erosion (James et al., 2001), suggesting rapid eustatic sea-level rise/basin subsidence outpaced by isostatic re-equilibration (Shields, 2005). In contrast, the presence of paleomagnetic reversals in cap dolostones suggests that their deposition could have exceeded several tens of kyr (e.g. Li, 2000; Raub et al., 2007; Raub, 2008; Schmidt et al., 2009; Trindade et al., 2003), and in Nuccaleena Formation the most likely horizon of isostatic rebound exceeding glacioeustasy lies within the

"Seacliff sandstone" member, beneath solid cap dolostone (Raub et al., 2007).

Assuming that the Nuccaleena–Ol plume is global, its duration can be estimated based on the results of Sr–Mg isotope of the cap dolostones using a simple geochemical box model (Fig. 4A). In this model, we consider the Sr and Mg reservoirs of the plume and deep seawater (Fig. 4A), and the fluxes in and out these reservoirs including: 1) continental weathering input (cw); 2) dolomite precipitation sink (dp); 3) exchange between deep seawater (ds) and the plume (pl). Assuming a quasi-steady state for Mg and Sr isotope compositions of cap dolostones, the following equation may be obtained (the derivation is elaborated in the supplemental information):

$$f_{\mathrm{Mg}}^{dp} = f_{\mathrm{Mg}}^{cw} \cdot \frac{(\Delta^{26}\mathrm{Mg}_{cw-pl} + \Delta^{26}\mathrm{Mg}_{ds-pl} \cdot r_{f-\mathrm{Mg}})}{\Delta^{26}\mathrm{Mg}_{dp-pl}}$$

where $r_{f-\mathrm{Mg}} = \frac{f_{\mathrm{Mg}}^{ds}}{f_{\mathrm{Mg}}^{cw}}$, and $\delta^{26}\mathrm{Mg}_{\mathrm{A-B}}$ is the difference of $\delta^{26}\mathrm{Mg}_{\mathrm{DSM3}}$ values between phase/reservoir A and B. With the calculated f_{Mg}^{dp}, the duration of Stage-2 cap-dolostone deposition can be estimated. Values of the parameters are calculated in the SI, based on the parameters shown in Table S3.

A Monte Carlo simulation was conducted to model the duration of the plume, which is calculated for 10 million times based on the random values within the bounds for all parameters in Sections S3.1–S3.4. Our calculation shows that the most likely duration for the plume is ~10 kyr (mean of 13 kyr and mode of ~8.4 kyr), with a 95% confidence interval of 2.3 to 202 kyr (Fig. 4B). Convergence of the simulation is achieved after being tested by random sampling for 0.05, 0.1, 0.5, 1, 5, 10 and 50 million times (Fig. 4C). Note that all model parameters were constrained as conservatively as possible here. Thus, even though only two cap-dolostone sections have been considered in this study, the modeling results should be representative of most cap dolostones. As more information about these parameters becomes available, better constraints are possible using our approach.

A sensitivity test has been conducted to evaluate how each parameter affects the modeled mean durations (Table S4). The largest range of the modeled results is observed by allowing f_{Mg}^{cw} to vary within the proposed bound, while there is much less influence on the modeled results from any of other parameters. Although our box model assumes a global melt–water plume, the duration of a localized plume might not be so different from these estimates due to the proportional reduction in continental weathering flux, area of continental shelf and volume of ocean, which can be tested in future studies.

The modeling result is incompatible with very fast deposition hypotheses based upon anomalous sedimentary facies. It is consistent with or slightly longer than ocean circulation and ice-sheet meltdown models, but much shorter than proposed duration of cap-dolostone deposition based on paleomagnetic reversal inferences. The inconsistent estimates at >10 kyr timescales may be reconciled by the following considerations. First, only cap dolostones formed during Stage 2 (i.e. NG-II and Ol Cap dolostones) were deposited within a plume reaching a dynamically steady state, whereas our calculation has yet to quantify the durations in Stage 1 and Stage 3 as the plume was developing and destabilized, respectively. Therefore, the total period for cap-dolostone formation should be longer than that of the dynamically stable plume. Second, the calculated duration of stratification for the Permian ocean (Zhang et al., 2001) may not be applicable to the meltwater plume during the Marinoan deglaciation because of different paleogeographic configurations and climate states between the two time periods. For instance, the duration predicted by ocean circulation models (Zhang et al., 2002, 2001) could be underestimated during the Stage 2 of the Marinoan deglaciation since it increases with increasing freshwater influx to the ocean (Zhang et al., 2002). Third, the modeled rates for ice-sheet decay (Hoffman et al., 2007; Hyde et al., 2000) during deglaciation could be slower. During continent-scale deglaciation, an appreciable volume of icesheet could lie below sea level in an isostatic well (Ivins and James, 2005), which would slow down the flow of icestreams to the continental margin. Finally, of the three paleomagnetic reversals observed in Nuccaleena cap dolostones (Raub, 2008), only one is present in NG-II cap dolostones, permitting short lifespan of the meltwater plume and prolonged terminal deglacial onset and ultimate postglacial recovery. Therefore, we prefer a relatively short duration (~8 kyrs) for the dynamically stabilized plume, but a longer timescale for overall cap-dolostone deposition.

5. Conclusion

Least-altered Sr and Mg isotope signatures in Nuccaleena and Ol cap dolostones are extracted by the step-leaching experiments. The results could be explained by their formation in two chemically distinct solutions, a glacial meltwater plume enriched in radiogenic Sr, and a saline ocean residue with lower $^{87}\mathrm{Sr}/^{86}\mathrm{Sr}$ ratios. The meltwater plume model reshapes the interpretation of all geochemical signatures of cap dolostones (e.g., C, Sr, Mg and Ca isotopes), and provides new insights for the formation of cap dolostones. Moreover, a geochemical box model for Sr and Mg mass balances suggest that the meltwater plume, if global, persists for most likely ~8 kyrs. This precludes very fast cap deposition hypotheses; it is consistent with a variety of relatively rapid cap-dolostone deposition models, and it permits slow deposition models with specific demands upon secular evolution of deglacial–postglacial ocean water chemistry.

Acknowledgement

We would like to thank P. Hu for analytical assistance, J. Ague, H. Affek, K. Turekian, D. Rye and C. Skinner for discussion and advice. This manuscript is greatly benefited from the constructive comments of Dr. Dudas and two anonymous reviewers. This research is funded by Yale Start-Up grant to Z.W. and NSF fund OCE-0752492.

Appendix A. Supplementary material

Supplementary material related to this article can be found online at http://dx.doi.org/10.1016/j.epsl.2014.06.039.

References

Albarède, F., Telouk, P., Blichert-Toft, J., Boyet, M., Agranier, A., Nelson, B., 2004. Precise and accurate isotopic measurements using multiple-collector ICPMS. Geochim. Cosmochim. Acta 68, 2725–2744.

Allegre, C.J., Louvat, P., Gaillardet, J., Meynadier, L., Rad, S., Capmas, F., 2010. The fundamental role of island arc weathering in the oceanic Sr isotope budget. Earth Planet. Sci. Lett. 292, 51–56.

Allen, P.A., Hoffman, P.F., 2005. Extreme winds and waves in the aftermath of a Neoproterozoic glaciation. Nature 433, 123–127.

Bao, H.M., Lyons, J.R., Zhou, C.M., 2008. Triple oxygen isotope evidence for elevated CO_2 levels after a Neoproterozoic glaciation. Nature 453, 504–506.

Berner, E.K., 2012. Berner, R.A., Global Environment: Water, Air, and Geochemical Cycles. Princeton University Press.

Bristow, T.F., Kennedy, M.J., Derkowski, A., Droser, M.L., Jiang, G., Creaser, R.A., 2009. Mineralogical constraints on the paleoenvironments of the Ediacaran Doushantuo Formation. Proc. Natl. Acad. Sci. USA 106, 13190–13195.

Calver, C.R., Crowley, J.L., Wingate, M.T.D., Evans, D.A.D., Raub, T.D., Schmitz, M.D., 2013. Globally synchronous Marinoan deglaciation indicated by U–Pb geochronology of the Cottons Breccia, Tasmania, Australia. Geology 41, 1127–1130.

Christie-Blick, N., Dyson, I.A., Vonderborch, C.C., 1995. Sequence stratigraphy and the interpretation of Neoproterozoic earth history. Precambrian Res. 73, 3–26.

Condon, D., Zhu, M.Y., Bowring, S., Wang, W., Yang, A.H., Jin, Y.G., 2005. U–Pb ages from the neoproterozoic Doushantuo Formation, China. Science 308, 95–98.

Davis, A.C., Bickle, M.J., Teagle, D.A., 2003. Imbalance in the oceanic strontium budget. Earth Planet. Sci. Lett. 211, 173–187.

Evans, D., Raub, T., 2011. Neoproterozoic glacial palaeolatitudes: a global update. Mem. Geol. Soc. Lond. 36, 93–112.

Fairchild, I.J., Kennedy, M.J., 2007. Neoproterozoic glaciation in the earth system. J. Geol. Soc. (Lond.) 164, 895–921.

Fantle, M.S., DePaolo, D.J., 2005. Variations in the marine Ca cycle over the past 20 million years. Earth Planet. Sci. Lett. 237, 102–117.

Font, E., Nédélec, A., Trindade, R., Moreau, C., 2010. Fast or slow melting of the Marinoan snowball Earth? The cap dolostone record. Palaeogeogr. Palaeoclimatol. Palaeoecol. 295, 215–225.

Gaillardet, J., Dupré, B., Louvat, P., Allègre, C.J., 1999. Global silicate weathering and CO_2 consumption rates deduced from the chemistry of large rivers. Chem. Geol. 159, 3–30.

Galy, A., Bar-Matthews, M., Halicz, L., O'Nions, R.K., 2002. Mg isotopic composition of carbonate: insight from speleothem formation. Earth Planet. Sci. Lett. 201, 105–115.

Galy, A., Yoffe, O., Janney, P.E., Williams, R.W., Cloquet, C., Alard, O., Halicz, L., Wadhwa, M., Hutcheon, I.D., Ramon, E., 2003. Magnesium isotope heterogeneity of the isotopic standard SRM980 and new reference materials for magnesium-isotope-ratio measurements. J. Anal. At. Spectrom. 18, 1352–1356.

Geske, A., Zorlu, J., Richter, D.K., Buhl, D., Niedermayr, A., Immenhauser, A., 2012. Impact of diagenesis and low grade metamorphosis on isotope (δ^{26}Mg, δ^{13}C, δ^{18}O and ^{87}Sr/^{86}Sr) and elemental (Ca, Mg, Mn, Fe and Sr) signatures of Triassic sabkha dolomites. Chem. Geol. 332–333, 45–64.

Halverson, G.P., Dudas, F.O., Maloof, A.C., Bowring, S.A., 2007. Evolution of the ^{87}Sr/^{86}Sr composition of Neoproterozoic seawater. Palaeogeogr. Palaeoclimatol. Palaeoecol. 256, 103–129.

Higgins, J.A., Schrag, D.P., 2003. Aftermath of a snowball Earth. Geochem. Geophys. Geosyst. 4.

Higgins, J.A., Schrag, D.P., 2010. Constraining magnesium cycling in marine sediments using magnesium isotopes. Geochim. Cosmochim. Acta 74, 5039–5053.

Hodell, D.A., Mead, G.A., Mueller, P.A., 1990. Variation in the strontium isotopic composition of seawater (8 Ma to present): implications for chemical weathering rates and dissolved fluxes to the oceans. Chem. Geol., Isot. Geosci. Sect. 80, 291–307.

Hoffmann, K.H., Condon, D.J., Bowring, S.A., Crowley, J.L., 2004. U–Pb zircon date from the Neoproterozoic Ghaub Formation, Namibia: constraints on Marinoan glaciation. Geology 32, 817–820.

Hoffman, P.F., 2011a. 'Glacial Lake Harland' and the calcium isotope record of the Marinoan glaciation. In: 2011 GSA Annual Meeting in Minneapolis.

Hoffman, P.F., 2011b. Strange bedfellows: glacial diamictite and cap carbonate from the Marinoan (635 Ma) glaciation in Namibia. Sedimentology 58, 57–119.

Hoffman, P.F., Li, Z.-X., 2009. A palaeogeographic context for Neoproterozoic glaciation. Palaeogeogr. Palaeoclimatol. Palaeoecol. 277, 158–172.

Hoffman, P.F., Schrag, D.P., 2002. The snowball Earth hypothesis: testing the limits of global change. Terra Nova 14, 129–155.

Hoffman, P.F., Halverson, G.P., Domack, E.W., Husson, J.M., Higgins, J.A., Schrag, D.P., 2007. Are basal Ediacaran (635 Ma) post-glacial "cap dolostones" diachronous? Earth Planet. Sci. Lett. 258, 114–131.

Hoffman, P.F., Kaufman, A.J., Halverson, G.P., Schrag, D.P., 1998. A Neoproterozoic Snowball Earth. Science 281, 1342–1346.

Hoffman, P.F., Macdonald, F.A., Halverson, G.P., 2011. Chemical sediments associated with Neoproterozoic glaciation: iron formation, cap carbonate, barite and phosphorite. Mem. Geol. Soc. Lond. 36, 67–80.

Huh, Y., Chan, L.-H., Zhang, L., Edmond, J.M., 1998. Lithium and its isotopes in major world rivers: implications for weathering and the oceanic budget. Geochim. Cosmochim. Acta 62, 2039–2051.

Hurtgen, M.T., Halverson, G.P., Arthur, M.A., Hoffman, P.F., 2006. Sulfur cycling in the aftermath of a 635-Ma snowball glaciation: evidence for a syn-glacial sulfidic deep ocean. Earth Planet. Sci. Lett. 245, 551–570.

Hyde, W.T., Crowley, T.J., Baum, S.K., Peltier, W.R., 2000. Neoproterozoic 'snowball Earth' simulations with a coupled climate/ice-sheet model. Nature 405, 425–429.

Ivins, E.R., James, T.S., 2005. Antarctic glacial isostatic adjustment: a new assessment. Antarct. Sci. 17, 541–553.

Jacobsen, S.B., Kaufman, A.J., 1999. The Sr, C and O isotopic evolution of Neoproterozoic seawater. Chem. Geol. 161, 37–57.

James, N.P., Narbonne, G.M., Kyser, T.K., 2001. Late Neoproterozoic cap carbonates: Mackenzie Mountains, northwestern Canada: precipitation and global glacial meltdown. Canad. J. Earth Sci. 38, 1229–1262.

Jiang, G., Kennedy, M.J., Christie-Blick, N., 2003. Stable isotopic evidence for methane seeps in Neoproterozoic postglacial cap carbonates. Nature 426, 822–826.

Kasemann, S.A., Hawkesworth, C.J., Prave, A.R., Fallick, A.E., Pearson, P.N., 2005. Boron and calcium isotope composition in Neoproterozoic carbonate rocks from Namibia: evidence for extreme environmental change. Earth Planet. Sci. Lett. 231, 73–86.

Kennedy, M.J., Christie-Blick, N., 2011. Condensation origin for Neoproterozoic cap carbonates during deglaciation. Geology 39, 319–322.

Kennedy, M.J., Christie-Blick, N., Prave, A.R., 2001a. Carbon isotopic composition of Neoproterozoic glacial carbonates as a test of paleoceanographic models for snowball Earth phenomena. Geology 29, 1135–1138.

Kennedy, M.J., Christie-Blick, N., Sohl, L.E., 2001b. Are Proterozoic cap carbonates and isotopic excursions a record of gas hydrate destabilization following Earth's coldest intervals? Geology 29, 443–446.

Kennedy, M., Mrofka, D., von der Borch, C., 2008. Snowball Earth termination by destabilization of equatorial permafrost methane clathrate. Nature 453, 642–645.

Kirschvink, J.L., 1992. Late Proterozoic low-latitude global glaciation: the Snowball Earth. In: Schopf, J.W., Klein, C. (Eds.), The Proterozoic Biosphere. Cambridge University Press, pp. 51–52.

Kennedy, M.J., Runnegar, B., Prave, A.R., Hoffmann, K.H., Arthur, M.A., 1998. Two or four Neoproterozoic glaciations? Geology 26, 1059–1063.

Kravchinsky, V.A., Sklyarov, E.V., Gladkochub, D.P., Harbert, W.P., 2010. Paleomagnetism of the Precambrian Eastern Sayan rocks: implications for the Ediacaran–Early Cambrian paleogeography of the Tuva–Mongolian composite terrane. Tectonophysics 486, 65–80.

Kunzmann, M., Halverson, G.P., Sossi, P.A., Raub, T.D., Payne, J.L., Kirby, J., 2013. Zn isotope evidence for immediate resumption of primary productivity after snowball Earth. Geology 41, 27–30.

Lamb, M.P., Fischer, W.W., Raub, T.D., Perron, J.T., Myrow, P.M., 2012. Origin of giant wave ripples in snowball Earth cap carbonate. Geology 40, 827–830.

Li, W., Chakraborty, S., Beard, B.L., Romanek, C.S., Johnson, C.M., 2012. Magnesium isotope fractionation during precipitation of inorganic calcite under laboratory conditions. Earth Planet. Sci. Lett. 333, 304–316.

Li, Z., 2000. New palaeomagnetic results from the 'cap dolomite' of the Neoproterozoic Walsh tillite, northwestern Australia. Precambrian Res. 100, 359–370.

Li, Z.-X., Evans, D.A., Halverson, G.P., 2013. Neoproterozoic glaciations in a revised global palaeogeography from the breakup of Rodinia to the assembly of Gondwanaland. Sediment. Geol. 294, 219–232.

Liu, C., Wang, Z., Raub, T.D., 2013. Geochemical constraints on the origin of Marinoan cap dolostones from Nuccaleena Formation, South Australia. Chem. Geol. 351, 95–104.

Macdonald, F.A., 2011. The Tsagaan Oloom Formation, southwestern Mongolia. Mem. Geol. Soc. Lond. 36, 331–337.

Macdonald, F.A., Jones, D.S., Schrag, D.P., 2009. Stratigraphic and tectonic implications of a newly discovered glacial diamictite-cap carbonate couplet in southwestern Mongolia. Geology 37, 123–126.

Mavromatis, V., Gautier, Q., Bosc, O., Schott, J., 2013. Kinetics of Mg partition and Mg stable isotope fractionation during its incorporation in calcite. Geochim. Cosmochim. Acta 114, 188–203.

McKirdy, D.M., Burgess, J.M., Lemon, N.M., Yu, X., Cooper, A.M., Gostin, V.A., Jenkins, R.J.F., Both, R.A., 2001. A chemostratigraphic overview of the late Cryogenian interglacial sequence in the Adelaide Fold-Thrust Belt, South Australia. Precambrian Res. 106, 149–186.

Pearce, C.R., Saldi, G.D., Schott, J., Oelkers, E.H., 2012. Isotopic fractionation during congruent dissolution, precipitation and at equilibrium: evidence from Mg isotopes. Geochim. Cosmochim. Acta 92, 170–183.

Preiss, W.V., 2000. The Adelaide Geosyncline of South Australia and its significance in Neoproterozoic continental reconstruction. Precambrian Res. 100, 21–63.

Raub, T., Evans, D., Smirnov, A., 2007. Siliciclastic prelude to Elatina–Nuccaleena deglaciation: lithostratigraphy and rock magnetism of the base of the Ediacaran system. Geol. Soc. (Lond.) Spec. Publ. 286, 53–76.

Raub, T.D., 2008. Prolonged deglaciation of "Snowball Earth". Yale University, 296 pp.

Roberts, J.A., Bennett, P.C., González, L.A., Macpherson, G., Milliken, K.L., 2004. Microbial precipitation of dolomite in methanogenic groundwater. Geology 32, 277–280.

Rooney, A.D., Macdonald, F.A., Strauss, J.V., Dudás, F.Ö., Hallmann, C., Selby, D., 2014. Re–Os geochronology and coupled Os–Sr isotope constraints on the Sturtian snowball Earth. Proc. Nat. Acad. Sci. 111, 51–56.

Rose, C.V., Maloof, A.C., 2010. Testing models for post-glacial 'cap dolostone' deposition: Nuccaleena formation, South Australia. Earth Planet. Sci. Lett. 296, 165–180.

Saenger, C., Wang, Z., 2014. Magnesium isotope fractionation in biogenic and abiogenic carbonates: implications for paleoenvironmental proxies. Quat. Sci. Rev. 90, 1–21.

Sánchez-Román, M., Vasconcelos, C., Schmid, T., Dittrich, M., McKenzie, J.A., Zenobi, R., Rivadeneyra, M.A., 2008. Aerobic microbial dolomite at the nanometer scale: implications for the geologic record. Geology 36, 879–882.

Schauble, E.A., 2011. First-principles estimates of equilibrium magnesium isotope fractionation in silicate, oxide, carbonate and hexaaquamagnesium(2+) crystals. Geochim. Cosmochim. Acta 75, 844–869.

Schmidt, P.W., Williams, G.E., McWilliams, M.O., 2009. Palaeomagnetism and magnetic anisotropy of late Neoproterozoic strata, South Australia: implications for the palaeolatitude of late Cryogenian glaciation, cap carbonate and the Ediacaran System. Precambrian Res. 174, 35–52.

Shields, G.A., 2005. Neoproterozoic cap carbonates: a critical appraisal of existing models and the plumeworld hypothesis. Terra Nova 17, 299–310.

Shields, G.A., Deynoux, M., Strauss, H., Paquet, H., Nahon, D., 2007. Barite-bearing cap dolostones of the Taoudéni Basin, northwest Africa: sedimentary and isotopic evidence for methane seepage after a Neoproterozoic glaciation. Precambrian Res. 153, 209–235.

Tipper, E.T., Galy, A., Gaillardet, J., Bickle, M.J., Elderfield, H., Carder, E.A., 2006. The magnesium isotope budget of the modem ocean: constraints from riverine magnesium isotope ratios. Earth Planet. Sci. Lett. 250, 241–253.

Trindade, R., Font, E., D'Agrella-Filho, M., Nogueira, A., Riccomini, C., 2003. Low-latitude and multiple geomagnetic reversals in the Neoproterozoic Puga cap carbonate, Amazon craton. Terra Nova 15, 441–446.

Van Lith, Y., Warthmann, R., Vasconcelos, C., Mckenzie, J.A., 2003. Sulphate-reducing bacteria induce low-temperature Ca-dolomite and high Mg-calcite formation. Geobiology 1, 71–79.

Vance, D., Teagle, D.A.H., Foster, G.L., 2009. Variable Quaternary chemical weathering fluxes and imbalances in marine geochemical budgets. Nature 458, 493–496.

Vasconcelos, C., McKenzie, J.A., 1997. Microbial mediation of modern dolomite precipitation and diagenesis under anoxic conditions (Lagoa Vermelha, Rio de Janeiro, Brazil). J. Sediment. Res. 67, 378–390.

Vasconcelos, C., McKenzie, J.A., Bernasconi, S., Grujic, D., Tiens, A.J., 1995. Microbial mediation as a possible mechanism for natural dolomite formation at low temperatures. Nature 377, 220–222.

Wang, Z., Hu, P., Gaetani, G., Liu, C., Saenger, C., Cohen, A., Hart, S., 2013. Experimental calibration of Mg isotope fractionation between aragonite and seawater. Geochim. Cosmochim. Acta 102, 113–123.

Warren, J., 2000. Dolomite: occurrence, evolution and economically important associations. Earth-Sci. Rev. 52, 1–81.

Warthmann, R., van Lith, Y., Vasconcelos, C., McKenzie, J.A., Karpoff, A.M., 2000. Bacterially induced dolomite precipitation in anoxic culture experiments. Geology 28, 1091–1094.

Williams, G.E., Gostin, V.A., McKirdy, D.M., Preiss, W.V., Schmidt, P.W., 2011. The Elatina glaciation (late Cryogenian), South Australia. Mem. Geol. Soc. Lond. 36, 713–721.

Zhang, F., Yan, C., Teng, H.H., Roden, E.E., Xu, H., 2012. *In situ* AFM observations of Ca–Mg carbonate crystallization catalyzed by dissolved sulfide: implications for sedimentary dolomite formation. Geochim. Cosmochim. Acta 105, 44–55.

Zhang, R., Follows, M.J., Grotzinger, J.P., Marshall, J., 2001. Could the Late Permian deep ocean have been anoxic? Paleoceanography 16, 317–329.

Zhang, R., Follows, M., Marshall, J., 2002. Mechanisms of thermohaline mode switching with application to warm equable climates. J. Climate 15, 2056–2072.

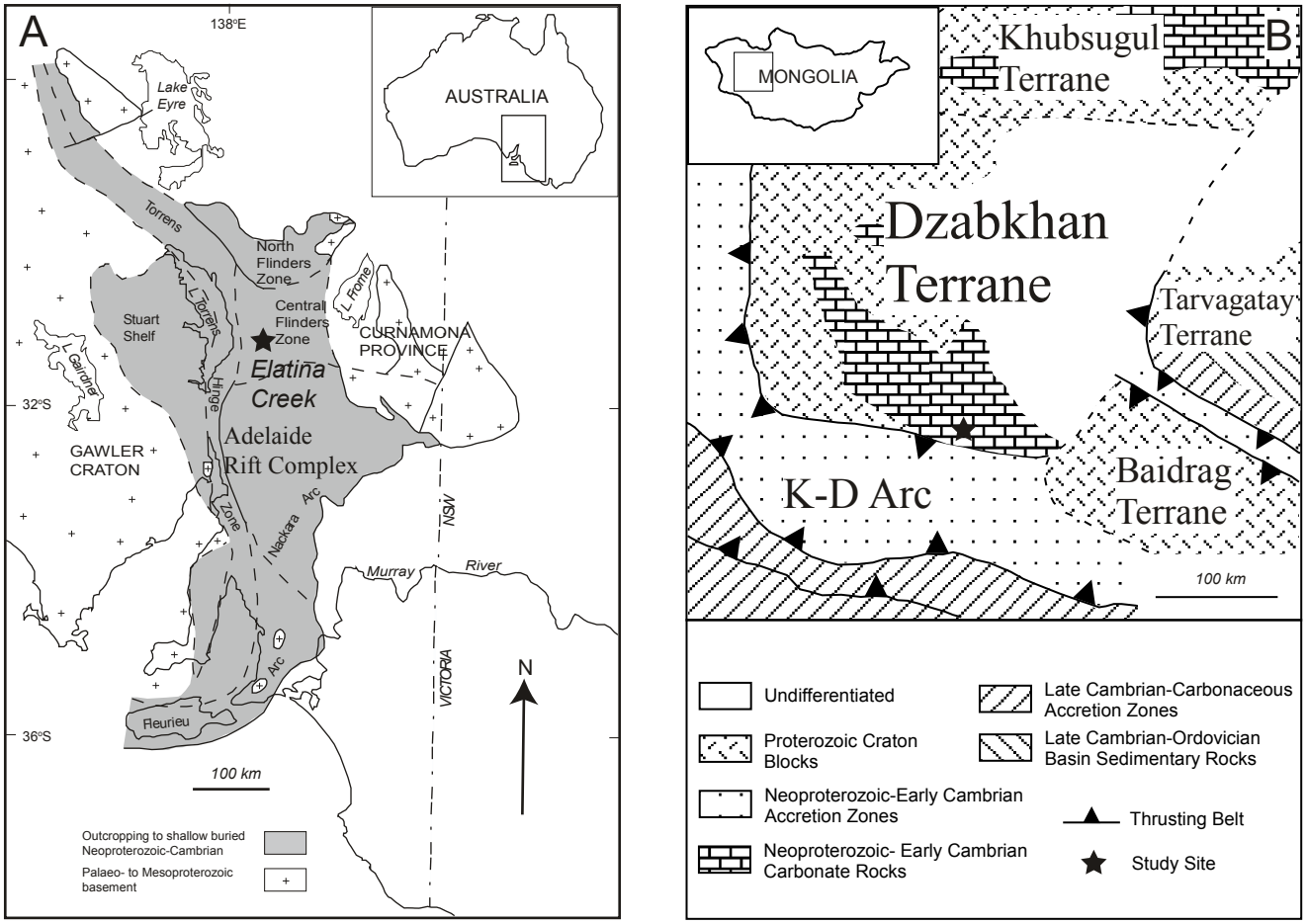
A
138°E
AUSTRALIA
Lake Eyre
Torrens
North Flinders Zone
Central Flinders Zone
Stuart Shelf
Elatina Creek
CURNAMONA PROVINCE
Adelaide Rift Complex
GAWLER CRATON
32°S
36°S
Fleurieu
Murray River
NSW
VICTORIA
N
100 km
Outcropping to shallow buried Neoproterozoic-Cambrian
Palaeo- to Mesoproterozoic basement
B
MONGOLIA
Khubsugul Terrane
Dzabkhan Terrane
Tarvagatay Terrane
Baidrag Terrane
K-D Arc
100 km
Undifferentiated
Proterozoic Craton Blocks
Neoproterozoic-Early Cambrian Accretion Zones
Neoproterozoic- Early Cambrian Carbonate Rocks
Late Cambrian-Carbonaceous Accretion Zones
Late Cambrian-Ordovician Basin Sedimentary Rocks
Thrusting Belt
Study Site

Fig. S1

Supplemental Information

S1 Brief geology background of the studied sites

Nuccaleena cap dolostones are collected from Adelaide Rift Complex (ARC) in South Australia (Fig. S1A). The ARC is thought to be part of an extensive continental margin, formed to the present-day east of the Stuart Shelf, where Neoproterozoic sediment accumulation is attributed to a succession of rift and thermal subsidence phases, with the main rifting commencing at ~827–802 Ma (e.g., Williams, 2008; Rose and Maloof, 2010). Ol cap dolostones in Southwest Mongolia are collected from the Dzabkhan terrane (Fig. S1B), which is a composite Precambrian terrane, hosting a heterogeneous Archean and Proterozoic crystalline basement intruded by ca. 800 Ma continental arc volcanism. The Dzabkhan basin is thought to be formed on segments of a ribbon continent that rifted away from Siberia in the late Neoproterozoic. Dzabkhan, Khubsugul, Baidrag and Tarvagatay terranes had amalgamated into a single continental mass by the Devonian (Macdonald et al., 2009 and references therein).

S2 Geochemical signatures of Ol limestones

We performed incremental leaching on all samples of Ol limestones overlying cap dolostones. Geochemical signatures in all leaching steps of selected samples (sample F708-44 and F708-64) were reported in Table S1. Calcite is the dominant mineral phase in all samples, indicated by low Mg/Ca ratios (Table S1) and scanning electron microscope (SEM-EDS) analysis. Nevertheless, partly-dolomitization is occasionally observed in some samples (e.g., F708-44), revealed by SEM-EDS analysis and Mg/Ca ratios in the last few leaching steps.

Geochemistry of Ol limestones is very complicated and deserves a separate paper to

elaborate (Liu et al., in prep). However, we can compare the average geochemical signatures of these limestones with cap dolostones. They exhibit significantly lower $^{87}Sr/^{86}Sr$ (~0.7079 on average) and $\delta^{26}Mg_{DSM3}$ (~ -2.95‰ on average) but similar Mn/Sr (~6mol/mol on average) compared to Ol cap dolostones. In addition, the most dolomitic components in partly-dolomitized samples exhibit higher Mn/Sr (50mol/mol) and lower $^{87}Sr/^{86}Sr$ ratios (0.7083), slightly higher $\delta^{26}Mg_{DSM3}$ (-1.62‰) than Ol cap dolostones. These different geochemical signatures (refer to Fig. 2) suggest that partly-dolomitized Ol limestones are the results of infiltration of diagenetic fluid with radiogenic $^{87}Sr/^{86}Sr$ and high $\delta^{26}Mg$ values through Ol limestones, and dolomites in them have different origins from Ol cap-dolostones.

S3. Derivation of equations for box-model

In the box model, we consider the Sr and Mg reservoirs of the plume and deep seawater (Fig. 4A), and the fluxes in and out these reservoirs including: 1) continental weathering input (cw); 2) dolomite precipitation sink (dp); 3) exchange between deep seawater (ds) and the plume (pl). Assuming a quasi-steady state for Mg and Sr isotope compositions of cap dolostones, variations of their isotopic compositions and mass with time should follow:

$$\begin{aligned}\frac{d(R_i^{pl}\cdot M_i^{pl})}{dt} &= R_i^{pl}\cdot\frac{d(M_i^{pl})}{dt} + M_i^{pl}\cdot\frac{d(R_i^{pl})}{dt} \\ &= R_i^{cw}\cdot f_i^{cw} - R_i^{dp}\cdot f_i^{dp} + R_i^{ds}\cdot f_i^{ds} - R_i^{pl}\cdot f_i^{pl}\end{aligned} \quad \text{(S.0)}$$

and

$$\frac{d(M_i^{pl})}{dt} = f_i^{cw} - f_i^{dp} + f_i^{ds} - f_i^{pl} \quad \text{(S.0)}$$

where R_i is isotopic ratios, $^{87}Sr/^{86}Sr$ or $^{26}Mg/^{24}Mg$. M_i is the mass of Sr or Mg in the plume. f_i is the flux of Mg or Sr to and from various reservoirs.

During Stage 2, $^{87}Sr/^{86}Sr$ or $^{26}Mg/^{24}Mg$ are roughly invariant. Hence $\frac{d(R_i^{pl})}{dt} \approx 0$.

Substituting $\frac{d(M_i^{pl})}{dt}$ by Eqn. (S2), Eqn. (S1) can be rewritten as Eqn. (S3):

$$(R_i^{pl} - R_i^{cw}) \cdot f_i^{cw} + (R_i^{pl} - R_i^{ds}) \cdot f_i^{ds} = (R_i^{pl} - R_i^{dp}) \cdot f_i^{dp} \quad \text{(S.0)}$$

For Sr isotopes, $(^{87}Sr/^{86}Sr)_{pl}=(^{87}Sr/^{86}Sr)_{dp}$, therefore, Eqn. (S3) can be rewritten as Eqn. (S4):

$$r_{f-Sr} = \frac{f_{Sr}^{ds}}{f_{Sr}^{cw}} = \frac{R_{Sr}^{cw} - R_{Sr}^{pl}}{R_{Sr}^{pl} - R_{Sr}^{ds}} \quad \text{(S.1)}$$

For Mg isotopes, Eqn. (S3) can be rewritten as Eqn. (S5):

$$f_{Mg}^{dp} = f_{Mg}^{cw} \cdot \frac{(\Delta^{26}Mg_{cw-pl} + \Delta^{26}Mg_{ds-pl} \cdot \eta_{Mg-Sr} \cdot r_{f-Sr})}{\Delta^{26}Mg_{dp-pl}} \quad \text{(S.2)}$$

In which $\eta_{Mg-Sr} = r_{f-Mg} / r_{f-Sr} = \frac{f_{Mg}^{ds}}{f_{Mg}^{cw}} \Big/ \frac{f_{Sr}^{ds}}{f_{Sr}^{cw}} = \frac{[Mg/Sr]_{ds}}{[Mg/Sr]_{cw}}$, and $\Delta^{26}Mg_{A\text{-}B}$ is the Mg isotope fractionation factor between A and B.

S4. Evaluation of model parameters.

S4.1 Evaluation of r_{f-Sr} and η_{Mg-Sr}

r_{f-Sr} can be calculated based on Eq. (S4) and parameters in Table S3, varying from 0 to 3.14. For $\eta_{Mg-Sr} = \frac{[Mg/Sr]_{ds}}{[Mg/Sr]_{cw}}$, $[Mg/Sr]_{cw}$ and $[Mg/Sr]_{ds}$ need to be evaluated separately. The continental weathering Mg/Sr ratios ($[Mg/Sr]_{cw}$) in the Neoproterozoic is proposed to be similar to modern values (~171, Gaillardet et al., 1999b), supported by the similar behavior of Mg and Sr during silicate weathering (Gislason et al., 1996; Nesbitt and Markovics, 1980). However, the seawater Mg/Sr ($[Mg/Sr]_{ds}$) could be significantly reduced compared to modern values, because during global glaciations without continental weathering input, the seawater Sr concentration would be maintained via carbonate dissolution and hydrothermal exchange (Higgins and Schrag, 2003), while Mg would be sequestrated by hydrothermal vents (Elderfield and Schultz, 1996; Tipper et al., 2006). Two bounds can be put on this value considering following two extreme cases: 1) there is no Mg left in the deep seawater, thus

$[Mg/Sr]_{ds} = 0$; and 2) $[Mg/Sr]_{ds}$ maintains a modern ocean value in spite of the hydrothermal sequestration. Therefore, η_{Mg-Sr} could vary from 0 to 0.93.

S4.2 Evaluation of $\Delta^{26}Mg$

In Eq. (S5), $\Delta^{26}Mg_{dp\text{-}pl}$ is the fractionation factor between dolomite and the waterplume, which could range from -0.8 to -2.8‰ (0 - 50°C), bounded by experimentally calibrated $\Delta^{26}Mg_{magnesite\text{-}solution}$ (Pearce et al., 2012) and $\Delta^{26}Mg_{aragonite\text{-}solution}$ (Wang et al., 2013). $\Delta^{26}Mg_{ds\text{-}pl}$ could be represented by the $\delta^{26}Mg$ difference between Stage-1 and Stage-2 cap dolostones, varying from -0.5 to -0.2 ‰, assuming that the cap dolostones formed at similar temperature and precipitation rates. $\Delta^{26}Mg_{cw\text{-}pl} = \delta^{26}Mg_{cw} - \delta^{26}Mg_{pl}$, in which $\delta^{26}Mg_{pl}$ is calculated based on $\delta^{26}Mg_{dp}$ and $\Delta^{26}Mg_{dp\text{-}pl}$, ranging from -1.0 to 1.0‰. $\delta^{26}Mg_{cw}$ should be dominated by silicate weathering, as indicated by the high $^{87}Sr/^{86}Sr$ ratios. Silicate-weathering rivers exhibit $\delta^{26}Mg_{cw}$ varying from -1.0 to +0.8 per mil (e.g. Pogge von Strandmann et al., 2008; Tipper et al., 2006), the majority of which are between -1.0 and -0.5‰. The current value $\Delta^{26}Mg_{cw\text{-}seawater}$ is about -0.2‰. During Stage 2, $\Delta^{26}Mg_{cw\text{-}pl}$ could be much lower compared to the modern $\Delta^{26}Mg_{cw\text{-}seawater}$ due to the widespread precipitation of dolomite, preferentially incorporation light Mg isotopes. Therefore, we propose $\Delta^{26}Mg_{cw\text{-}pl}$ varies from -0.2 to -2.0‰.

S4.3 Evaluation of f_{Mg}^{cw}

In previous studies, cap dolostones are proposed to deposit during deglaciation and when carbonate weathering is dominant (Higgins and Schrag, 2003), while silicate weathering only became significant after cap-dolostone deposition and the deglaciation (Higgins and Schrag, 2003; Le Hir et al., 2009). However, the elevated Sr and Mg isotope signals in Stage-2 cap dolostones suggest that silicate weathering could be dominant during Stage 2 (Kennedy et al., 2001a). The silicate weathering fluxes mainly depend on dissolution rate of silicate minerals (R_{diss}) and surface runoffs. The modeled R_{diss} values in a post-glacial greenhouse environment are similar, which are ~6-8 times of modern values (Fabre et al., 2011; Le Hir et al., 2009). In

comparison, the modeled surface runoffs could vary from 1.2 to 7 times of modern values (Higgins and Schrag, 2003; Le Hir et al., 2009), therefore, the modeled continental weathering rates range from ten (Le Hir et al., 2009) to fifty (Lee Kump, personal communication in Higgins and Schrag, 2003) times of modern values. However, this range could be even larger. The weathering rate at low temperatures by glacial meltwater could be comparable to modern values (Le Hir et al., 2009), while it could be much larger at higher temperatures if glacial meltwater fluxes were equivalent to ~16 times of modern runoffs (Hoffman, 2011a). Considering both glacial meltwater fluxes and river runoffs, a more conservative estimation of the continental weathering flux would thus be from 1 to 200 times of modern values.

S4.4 Evaluation of the amount of Stage-2 cap dolostones

The total amount Mg sequestrated by Stage-2 cap dolostones (N_{Mg}) can be calculated if the average thickness (D) and the deposition area (A) of Stage-2 cap dolostones are known. We allow D to vary from 2.5 to 6 m, which are the observed thickness of NG-II and Ol Cap dolostones; and A is permitted to vary from 28% (about the area of modern continental margin) to 16% (a lower value due to a shallower carbonate compensation depth in a super greenhouse environment, Hoffman et al., 1998; Bao et al., 2008; and the presence of epicontinental seas, Li et al., 2013). In addition, we assume a low porosity (0-0.1) for the cap dolostones (Lamb et al., 2012).

Table S1. $^{87}Sr/^{86}Sr$ (before Rb-decay correction), $\delta^{26}Mg_{DSM3}$(‰) and trace metal ratios of all leaching steps of two selected samples from Ol limestones, Mongolia

Step	F708-44					F708-64				
	$^{87}Sr/^{86}Sr$	$\delta^{26}Mg_{DSM3}$(‰)	Mg/Ca (mol/mol)	Mn/Sr (mol/mol)	Rb/Sr (mmol/mol)	$^{87}Sr/^{86}Sr$	$\delta^{26}Mg_{DSM3}$(‰)	Mg/Ca (mol/mol)	Mn/Sr (mol/mol)	Rb/Sr (mmol/mol)
N1	0.71008(3)	-1.98(8)	0.056(10)	2.0(10)	20.9(18)	0.70786(3)	-2.30(2)	0.012(1)	0.40(1)	0.92(8)
N2	0.70953(3)	-2.61(5)	0.020(8)	28.8(15)	11.3(20)	0.70774(2)	-2.78(3)	0.008(1)	0.96(2)	0.23(6)
S1	0.70910(3)	-3.10(4)	0.016(4)	9.6(2)	5.52(31)	0.70771(2)	-2.79(2)	0.007(2)	0.07(3)	0.047(15)
S2	0.70904(2)	-3.14(4)	0.014(3)	19.6(3)	5.52(31)	0.70766(2)	-2.72(1)	0.007(2)	0.44(2)	0.069(12)
S3	0.70900(3)	-3.16(7)	0.015(2)	18.3(4)	4.28(24)	0.70767(2)	-2.73(5)	0.007(1)	0.84(1)	0.075(7)
S4	0.70898(2)	-2.98(3)	0.016(3)	16.5(4)	2.50(14)	0.70766(2)	-2.61(2)	0.006(1)	0.73(1)	0.068(7)
S5	0.70893(2)	-2.99(1)	0.014(2)	17.2(4)	2.13(12)	0.70765(2)	-2.57(4)	0.006(1)	0.66(1)	0.061(7)
S6	0.70886(2)	-3.03(3)	0.014(3)	17.8(5)	1.45(8)	0.70762(2)	-2.57(1)	0.006(1)	0.59(1)	0.046(7)
S7	0.70871(2)	-1.96(2)	0.058(4)	20.4(5)	1.50(9)	0.70762(2)	-2.51(7)	0.006(1)	0.54(1)	0.041(6)
S8	0.70862(2)	-1.97(3)	0.093(2)	26.4(6)	1.56(9)	0.70761(2)	-2.57(1)	0.006(1)	0.56(1)	0.026(3)
S9	0.70841(2)	-1.75(2)	0.206(4)	36.6(6)	2.03(12)	0.70764(2)	-2.20(1)	0.015(2)	0.70(2)	0.048(6)
S10	0.70835(4)	-1.70(4)	0.208(4)	38.5(3)	1.35(8)	0.70761(2)	-1.80(4)	0.016(2)	0.69(2)	0.050(5)
S11	0.70847(4)	-1.89(4)	0.144(3)	32.2(4)	3.00(17)	0.70762(2)	-1.63(5)	0.063(7)	0.96(7)	0.126(18)
S12	0.70832(7)	-1.62(4)	0.455(4)	52.6(9)	5.13(86)	0.70770(2)	-1.43(1)	0.64(3)	5.7(6)	0.86(15)
S13	0.70940(4)	-1.56(3)	0.393(50)	43.9(12)	18.3(93)	0.70769(2)	-1.31(3)	0.72(3)	5.9(8)	2.33(28)

Table S2. Modeling Parameters to calculate Stage-Two duration

Parameters	Values	Reference
$(^{87}Sr/^{86}Sr)_{cw}$	0.7089 - 0.7135	(Higgins and Schrag, 2003; Kennedy et al., 2001a)
$(^{87}Sr/^{86}Sr)_{ds}$	0.7071	(Halverson et al., 2007)
$\Delta^{26}Mg_{cw\text{-}pl}$(‰)	-2.0 ~ -0.2	(Pogge von Strandmann et al., 2008; Saenger and Wang, 2014; Tipper et al., 2006)
$\Delta^{26}Mg_{dp\text{-}pl}$ (‰)	-3.0 ~ -2.0	(Li et al., 2012; Pearce et al., 2012; Saenger and Wang, 2014; Wang et al., 2013)
$\Delta^{26}Mg_{ds\text{-}pl}$ (‰)	-0.5 ~ -0.2	
$(Mg/Sr)_{cw\text{-}ppm}$	171	(Gaillardet et al., 1999a; Gaillardet et al., 1999b)
$(Mg/Sr)_{ds\text{-}ppm}$	0 - 159	
D (meter)	2.5 - 6	
A (% of modern ocean area)	16 - 28	(Li et al., 2013)
Modern $f_{Mg\text{-}cw}$ (Tmol/yr)	5.6	(Tipper et al., 2006)

Table S3. Range of the modeled mean durations by allowing each parameter to vary within the proposed bounds.

	Minimum(kys)	Maximum(kys)
f_{cw}	4.9	974
$r_{f\text{-}Mg}$	9.3	20
$\Delta^{26}Mg_{dp\text{-}pl}$	6.1	21
$\Delta_{26}Mg_{ds\text{-}pl}$	11	15
$\Delta_{26}Mg_{cw\text{-}pl}$	7.6	30
D	7.8	19
A	9	16
porosity	12	14

Figure Captions

Fig. S1. A: Geologic map of ARC in South Australia, based on Williams (2008); B: Geologic map of Dzabkhan Terrane in Southwest Mongolia, based on Macdonald (2009).

References

Bao, H.M., Lyons, J.R., Zhou, C.M., 2008. Triple oxygen isotope evidence for elevated CO(2) levels after a Neoproterozoic glaciation. Nature 453, 504-506.
Elderfield, H., Schultz, A., 1996. Mid-ocean ridge hydrothermal fluxes and the chemical composition of the ocean. Annu Rev Earth Pl Sc 24, 191-224.
Fabre, S., Berger, G., Nédélec, A., 2011. Modeling of continental weathering under high‐CO2 atmospheres during Precambrian times. Geochemistry, Geophysics, Geosystems 12.
Gaillardet, J., Dupre, B., Allegre, C.J., 1999a. Geochemistry of large river suspended sediments: Silicate weathering or recycling tracer? Geochim Cosmochim Ac 63, 4037-4051.
Gaillardet, J., Dupré, B., Louvat, P., Allègre, C.J., 1999b. Global silicate weathering and CO2 consumption rates deduced from the chemistry of large rivers. Chemical Geology 159, 3-30.
Gislason, S.R., Arnorsson, S., Armannsson, H., 1996. Chemical weathering of basalt in Southwest Iceland; effects of runoff, age of rocks and vegetative/glacial cover. American Journal of Science 296, 837-907.
Halverson, G.P., Dudas, F.O., Maloof, A.C., Bowring, S.A., 2007. Evolution of the Sr-87/Sr-86 composition of Neoproterozoic seawater. Palaeogeogr Palaeocl 256, 103-129.
Higgins, J.A., Schrag, D.P., 2003. Aftermath of a snowball Earth. Geochem Geophy Geosy 4, -.
Hoffman, P.F., 2011a. 'Glacial Lake Harland' and the calcium isotope record of the Marinoan glaciation. 2011 GSA Annual Meeting in Minneapolis.
Hoffman, P.F., Kaufman, A.J., Halverson, G.P., Schrag, D.P., 1998. A Neoproterozoic snowball earth. Science 281, 1342-1346.
Kennedy, M.J., Christie-Blick, N., Prave, A.R., 2001a. Carbon isotopic composition of Neoproterozoic glacial carbonates as a test of paleoceanographic models for snowball Earth phenomena. Geology 29, 1135-1138.
Lamb, M.P., Fischer, W.W., Raub, T.D., Perron, J.T., Myrow, P.M., 2012. Origin of giant wave ripples in snowball Earth cap carbonate. Geology 40, 827-830.
Le Hir, G., Donnadieu, Y., Goddéris, Y., Pierrehumbert, R.T., Halverson, G.P., Macouin, M., Nédélec, A., Ramstein, G., 2009. The snowball Earth aftermath: Exploring the limits of continental weathering processes. Earth Planet Sc Lett 277, 453-463.
Li, Z.-X., Evans, D.A., Halverson, G.P., 2013. Neoproterozoic glaciations in a revised global palaeogeography from the breakup of Rodinia to the assembly of Gondwanaland. Sedimentary Geology 294, 219-232.
Macdonald, F.A., Jones, D.S., Schrag, D.P., 2009. Stratigraphic and tectonic implications of a newly discovered glacial diamictite-cap carbonate couplet in southwestern Mongolia. Geology 37, 123-126.
Nesbitt, H.W., Markovics, G., 1980. Chemical processes affecting alkalis and alkaline earths during continental weathering. Geochim Cosmochim Ac 44, 1659-1666.
Pearce, C.R., Saldi, G.D., Schott, J., Oelkers, E.H., 2012. Isotopic fractionation during congruent dissolution, precipitation and at equilibrium: Evidence from Mg isotopes. Geochimica et Cosmochimica Acta.
Pogge von Strandmann, P.A., Burton, K.W., James, R.H., van Calsteren, P., Gislason, S.R., Sigfússon, B., 2008. The influence of weathering processes on riverine magnesium isotopes in a basaltic terrain. Earth Planet Sc Lett 276, 187-197.
Rose, C.V., Maloof, A.C., 2010. Testing models for post-glacial 'cap dolostone' deposition: Nuccaleena Formation, South Australia. Earth Planet Sci Lett 296, 165-180.
Saenger, C., Wang, Z., 2014. Magnesium isotope fractionation in biogenic and abiogenic carbonates: implications for paleoenvironmental proxies. Quaternary Science Reviews 90, 1-21.
Tipper, E.T., Galy, A., Gaillardet, J., Bickle, M.J., Elderfield, H., Carder, E.A., 2006. The magnesium isotope budget of the modem ocean: Constraints from riverine magnesium isotope ratios. Earth Planet Sci Lett 250, 241-253.
Wang, Z., Hu, P., Gaetani, G., Liu, C., Saenger, C., Cohen, A., Hart, S., 2013. Experimental calibration of Mg isotope fractionation between aragonite and seawater. Geochimica Et Cosmochimica Acta 102, 113-123.
Williams, G.E., Gostin, V.A., McKirdy, D.A., Preiss W.V., 2008. The Elatina glaciation, late Cryogenian (Marinoan Epoch), South Australia: sedimentary facies and palaeoenvironments. Precambrian Research, 163, 307–331